A PROJECT REPORT ON

Open Loop Speed Control of BLDC Motor for EV Applications.

For SUMMER INTERNSHIP PROGRAMME

Bachelor of Technology

in

Electrical and Electronics Engineering

Submitted by

A.VENKATA NAGA SAI TEJA (Reg.No. N200907)
P.PRAJNA (Reg.No. N200409)
T.KEERTHANA LAKSHMI (Reg.No. N200403)
R.ABHISHEK (Reg.No. N200839)

Under the supervision of

Dr. RANJAN KUMAR BEHERA
Dr. RANJEET MANDAL

DEPARTMENT OF ELECTRICAL ENGINEERING,
INDIAN INSTITUTE OF TECHNOLOGY, PATNA

DEPARTMENT OF ELECTRICAL AND ELECTRONICS ENGINEERING,
RAJIV GANDHI UNIVERSITY OF KNOWLEDGE TECHNOLOGIES, NUZVID

CERTIFICATE OF THE SUPERVISOR(S)

This is to certify that the project entitled **"Open Loop Speed Control of BLDC Motor for EV Applications."** being submitted to the Indian Institute of Technology, Patna, by**A.Venkata Naga Sai Teja(Reg. No. N200907) P.Prajna(Reg. No. N200409) T.Keerthana Lakshmi(Reg. No. N200403) R.Abhishek(Reg. No. N200839)** for the completed an internship program from **15/05/2025** to **15/07/2025**, is a bonafide work carried out by the team, in the Department of Electrical Engineering, IIT, Patna, under our supervision and guidance.

Dr. Ranjeet Mandal
Research Fellow
Department of Electrical Engineering,
Indian Institute of Technology, Patna

Dr. Ranjan Kumar Behera
Associate Professor
Department of Electrical Engineering,
Indian Institute of Technology, Patna

Acknowledgement

We would like to extend our deepest gratitude towards **Prof (Dr.) Ranjan Kumar Behera** and **Dr. Ranjeet Mandal** to the Department of Electrical Engineering, Indian Institute of Technology, Patna, for their valuable guidance, productive feedback, and endless support during the duration of this study. Their invaluable input and encouragement contributed significantly towards developing this study.

A.Venkata Naga Sai Teja
RGUKT IIIT,Nuzvid
July 15,2025

P.Prajna
RGUKT IIIT,Nuzvid
July 15,2025

T.Keerthana Lakshmi
RGUKT IIIT,Nuzvid
July 15,2025

R.Abhishek
RGUKT IIIT,Nuzvid
July 15,2025

Contents

List of abbreviations

Abbreviation	Description
AC	Alternating current
AVM	Average-value model
BLDC	Brushless direct current
CNC	Computerized numerical control
DC	Direct current
DTC	Direct torque control
DSP	Digital signal processor
EMF	Electromotive force
EMI	Electromagnetic interference
EV	Electric vehicle
FOC	Field-oriented control
HVAC	Heating, ventilation, and air conditioning
IEEE	Institute of electrical and electronics engineers
IGBT	Insulated-gate bipolar transistor
IN-C	Incremental conduction
IoT	Internet of things
MBD	Model-based design
MOSFET	Metal-oxide-semiconductor field-effect transistor
MPPT	Maximum power point tracking
PI	Proportional-integral
PLL	Phase-locked loop
PV	Photovoltaic
PWM	Pulse width modulation
SVPWM	Space vector pulse width modulation
VSI	Voltage source inverter

Chapter-I

Introduction

1 Introduction

1.1 Introduction to brushless DC motors

Brushless Direct Current (BLDC) motors have revolutionized modern electromechanical systems by merging the controllability of traditional DC motors with the reliability of AC induction machines. Unlike brushed DC motors, which rely on mechanical commutation through carbon brushes and commutators, BLDC motors employ electronic switching to achieve superior efficiency, precision, and longevity. This innovation eliminates brush-related wear, sparking, and electromagnetic interference, making them indispensable in applications demanding high performance and minimal maintenance [1][2].

The fundamental operation of BLDC motors hinges on the electromagnetic interaction between a stationary stator equipped with multiphase windings and a rotating permanent magnet rotor. Electronic commutation—orchestrated by a dedicated controller—sequentially energizes stator phases to generate a rotating magnetic field that propels the rotor. This process requires precise timing, typically guided by hall effect sensors or sensorless techniques that monitor back-electromotive force (EMF) zero-crossing events. The absence of physical brushes allows these motors to operate in harsh environments while maintaining consistent performance over extended periods.

Construction and components:
BLDC motors comprise three primary components: a laminated steel stator with precision-wound copper coils, a rotor embedded with high-energy rare-earth magnets (e.g., neodymium-iron-boron), and an electronic control unit. The stator windings are usually arranged in a three-phase star configuration, optimized for trapezoidal or sinusoidal back-EMF profiles. Depending on application requirements, the rotor may adopt an inner-rotor configuration (commonly used in industrial applications) or an outer-rotor design (favored in compact, high-torque systems). The electronic controller, consisting of power semiconductor switches such as MOSFETs or IGBTs, governs phase current delivery via pulse-width modulation (PWM) for precise torque and speed control [3].

Advantages over brushed motors:
BLDC motors outperform their brushed counterparts in several aspects, including higher efficiency (85–95%), increased power density, longer operational life, and reduced acoustic noise. Their brushless nature avoids frictional losses, minimizes arcing, and allows for silent operation—making them ideal for applications in aerospace, medical equipment, and personal electronics. Additionally, advanced digital control algorithms empower BLDC motors with features like regenerative braking, adaptive speed control, and seamless integration into IoT-enabled systems.

Emerging applications:
The rapid adoption of BLDC motors spans across industries—from electric vehicle propulsion systems to robotic actuators, CNC machinery, HVAC systems, and precision medical tools. Their robustness and ability to maintain stable performance under varying loads make them a top choice in smart manufacturing and renewable energy technologies. Continuous innovations in magnetic materials, power electronics, and control techniques further accelerate their relevance in next-generation electromechanical systems.

1.2 Block diagram of BLDC motor system

To better understand the interaction between electronic components and motor hardware, a functional block diagram of a BLDC drive system is shown in Figure 1. This schematic demonstrates how the controller processes Hall sensor signals to determine the rotor position and sequentially triggers gate signal of inverter, which includes six IGBT switches, provides three-phase power to the BLDC motor, enabling efficient commutation.

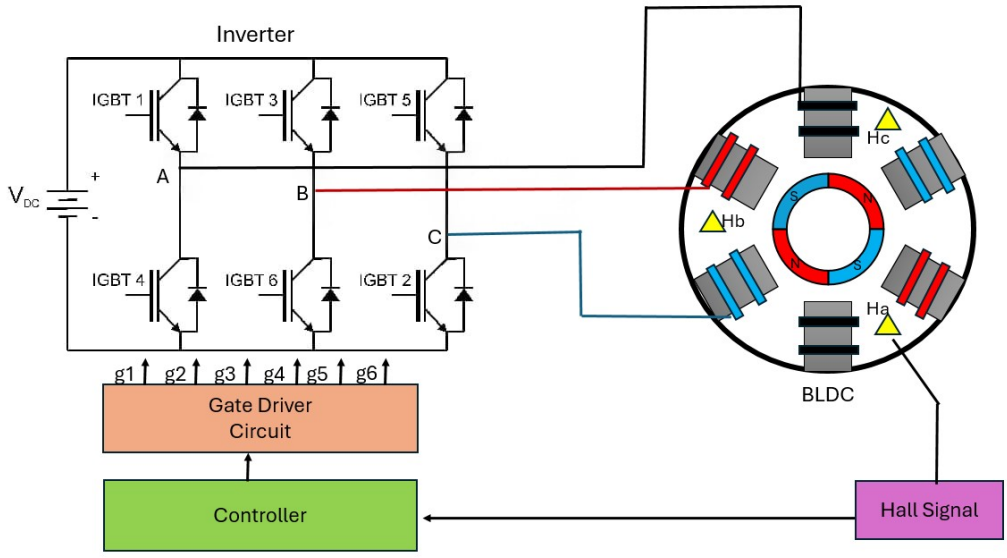

Fig. 1: Functional block diagram of a BLDC motor drive system

The system begins with the controller, which interprets position feedback from hall sensors (Ha, Hb, Hc) mounted inside the motor. Based on rotor position, the controller sends gate pulses (g1 to g6) to a gate driver circuit, which amplifies these signals and drives the appropriate IGBT switches in the three-phase inverter. This inverter converts DC supply into synchronized three-phase AC signals that energize the stator windings of the BLDC motor. The correct sequence of switching ensures that the rotor continues to follow the rotating magnetic field without stalling or misalignment.

This configuration is widely used in electric vehicles, drones, robotic arms, and high-speed industrial machinery, where precise torque control and high efficiency are mandatory. The closed-loop feedback mechanism using Hall signals also ensures dynamic adaptability to load changes and enhances the reliability of the drive system.

This introduction sets the stage for understanding the operating principles, structural innovations, and wide-ranging impact of BLDC motors—topics that are further explored throughout this report.

1.3 Objectives

The primary objective of this project is to develop, simulate, and experimentally validate a complete control and drive system for a Brushless DC (BLDC) motor using both open-loop and closed-loop

strategies. The goal is to build an accurate dynamic model, design suitable control algorithms, and implement the system in real time using both OPAL-RT and dSPACE 1104 hardware platforms. The specific objectives are:

- To derive and formulate the core electrical and mechanical equations of a three-phase BLDC motor, including phase voltage equations, line current dynamics, torque production, and rotor motion.
- To build a complete mathematical model in MATLAB/Simulink, integrating subsystems such as back-EMF generation, electromagnetic torque computation, and mechanical speed estimation.
- To model and simulate six-step inverter commutation under 120° conduction mode, using sector identification through Hall sensor decoding logic.
- To verify system behavior under open-loop conditions by analyzing back-EMF profiles, phase voltages, line currents, and rotor speed under both no-load and load scenarios.
- To perform real-time validation of the open-loop model using OPAL-RT (RT-LAB) simulation environment, verifying dynamic performance under realistic timing constraints and system latencies.
- To design a Proportional-Integral (PI) controller for outer-loop speed control, ensuring improved response, reduced steady-state error, and better load disturbance rejection.
- To simulate and evaluate system performance under speed reference steps and mechanical load perturbations, observing the closed-loop response of torque and speed.
- To implement the complete control algorithm on the dSPACE 1104 real-time platform, interfacing it with Hall sensors, gate driver circuits, an amplifier, and a three-phase inverter.
- To validate simulation outputs with oscilloscope-based measurements of line currents, voltages, and rotor speed during hardware operation.
- To demonstrate practical synchronization between Simulink-based logic and real-time gate signal generation using dSPACE and evaluate the system's dynamic stability.
- To lay the groundwork for advanced future enhancements including Direct Torque Control (DTC), Field-Oriented Control (FOC), sensorless methods, and torque ripple minimization techniques.

Chapter-II

Literature Review

2 Literature review

Zheng *et al.* [4] presents a detailed study of modeling comparison between different modeling approaches for BLDC motors. It analyzes mathematical, state-space, and Simulink-based models to evaluate dynamic behavior, back-EMF characteristics, and torque response. From this paper, we understood how different modeling techniques affect the accuracy of motor performance prediction and are crucial in selecting an appropriate control strategy for real-time applications. The paper emphasizes that while mathematical modeling offers foundational understanding, it often lacks the flexibility needed for complex system integration. On the other hand, state-space modeling enables multi-domain analysis and is suitable for linear control design, whereas Simulink-based modeling excels in simulation visualization and modular subsystem design. The study also demonstrates that modeling fidelity plays a significant role in closed-loop control effectiveness, especially when dealing with high-speed applications or torque ripple minimization. This comparison provided key insights that influenced the design and implementation approach of our own BLDC motor simulation framework.

Poovizhi *et al.* [5] investigated the mathematical modelling of BLDC drives using MATLAB-Simulink, focusing on the fundamental voltage and torque equations that govern motor dynamics. The paper presents a clear derivation of the electrical equations for each phase and incorporates back-EMF and electromagnetic torque expressions into the simulation framework. It provides detailed insights into rotor speed profiles, the nature of trapezoidal back-EMF waveforms, and torque response under varying load conditions. The MATLAB-Simulink implementation confirms that theoretical equations are consistent with practical simulation results, reinforcing the validity of classical motor models. The study also demonstrates how changes in load torque impact speed and current response, which is crucial for controller design. This research helped us understand how simulation-based verification strengthens confidence in analytical equations and lays a strong foundation for implementing both open-loop and closed-loop control strategies. The paper serves as a useful reference in replicating dynamic BLDC behavior in our own modeling and analysis.

Sithananthan *et al.* [6] designed and simulated a DC-DC buck-boost converter integrated with a voltage source inverter (VSI) using MATLAB/Simulink for BLDC motor drive applications. The study demonstrates an effective power conversion system in which the buck-boost converter regulates the input voltage to maintain consistent DC bus conditions, while the VSI performs phase commutation required for motor operation. The converter ensures that the BLDC motor receives stable voltage even during fluctuating input or variable load conditions. This is particularly vital in electric vehicle applications, where the power source (typically a battery) is subject to dynamic behavior. The paper highlights how proper interaction between the converter and motor drive system leads to enhanced efficiency, reduced torque ripple, and improved transient response. From this study, we understood the critical role of intermediate power electronics in optimizing the performance of BLDC motors and how accurate converter design directly impacts system reliability and motor control precision.

Babu *et al.* [7] present a detailed study on closed-loop speed control of BLDC motors using a flyback converter, specifically targeting electric vehicle (EV) applications. The paper implements a feedback-based control strategy in which the output of a flyback DC-DC converter is regulated based on the motor's speed error. The integration of the flyback converter with the control loop helps achieve effective voltage regulation and smooth operation across a wide range of load conditions. The study demonstrates improved dynamic response, minimal speed deviation, and reduced torque and current ripples compared to open-loop configurations. This is particularly significant in EVs, where performance consistency and energy efficiency are critical. From this work, we understood the practical advantages of closed-loop control in maintaining precise speed regulation, even under varying road or load conditions, and how converter-based regulation enhances both stability and system efficiency. The insights gained have guided our understanding of advanced control strategies in BLDC motor drives.

Yadunandan *et al.* [8] worked on modelling of bldc motor foc and hard-ware implementation using f28069m launchpad, presents a detailed study on the modeling and hardware implementation of FOC for a BLDC motor using MATLAB/Simulink and a Texas Instruments F28069M LaunchPad. The proposed system transforms the stator current to the d-q rotating reference frame using Clarke and Park transformations, enabling decoupled control of torque and flux components. A Model-Based Design (MBD) approach is utilized, where the simulation model is directly deployed onto the DSP controller. The authors employ PI controllers to regulate the d- and q-axis currents and generate PWM signals via SVPWM technique to drive the inverter. Rotor position estimation is achieved using Hall-effect sensors, and the hardware setup includes a 3-phase inverter, gate driver circuits, and LEM sensors for current feedback. Simulation results demonstrate accurate tracking of torque and speed, while hardware validation confirms the effectiveness of FOC in achieving smooth and efficient motor performance. From this paper, we learned how advanced control techniques like FOC, when combined with MBD, can enhance real-time performance and simplify the implementation of complex algorithms for BLDC motor drives.

Bondre *et al.* [9] conducted research on mathematical modeling of DTC of bldc motor, presents a detailed study on the application of DTC to BLDC motors, focusing on mathematical modeling and simulation in MATLAB/Simulink. The authors derive the voltage and torque equations of the BLDC motor and use them to develop a state-space model. The DTC strategy aims to reduce torque ripples by adjusting stator flux and torque within hysteresis bands using a switching table. Unlike conventional methods that rely on coordinate transformations, the DTC approach allows direct control of motor torque without needing position sensors, thereby reducing system complexity. The simulation results show the performance of torque and flux control in the - reference frame, highlighting the effectiveness of DTC in improving dynamic response. From this paper, we learned how mathematical modeling combined with DTC can provide high-efficiency, sensorless torque control for BLDC motors, particularly useful for electric vehicle and industrial drive systems.

Burman *et al.* [10] designed an efficient cuk converter for a bldc motor drive, presents the design and performance evaluation of a Cuk DC-DC converter feeding a BLDC motor drive, with a focus on closed-loop voltage regulation using a PI controller. The system architecture includes an AC mains input, a diode-based rectifier, a Cuk converter, a voltage source inverter (VSI), and a BLDC motor. The Cuk converter is chosen for its ability to produce a continuous input current and an inverting output voltage with lower ripple, making it suitable for precise motor control. The PI controller is used to maintain a reference voltage at the DC link, ensuring stable operation of the motor drive. Simulation studies conducted in MATLAB/Simulink demonstrate the steady-state, transient, and dynamic behavior of the motor under varying voltage conditions. From this paper, we learned how the Cuk converter, when integrated with a well-tuned PI controller and electronic commutation, offers an efficient and compact solution for smooth and stable operation of BLDC motors, with improved voltage regulation and dynamic response.

Sierra *et al.* [11] presented a detailed comparison of various switching techniques for BLDC motors, with a focus on sensored control using Hall effect sensors. The authors implemented a Simulink model using trapezoidal commutation to analyze torque behavior and speed control. The study reviews three primary switching methods: trapezoidal, sinusoidal, and vectorial commutation. Trapezoidal commutation, while simple and easy to implement, introduces a torque ripple of up to 15%, affecting low-speed performance. Sinusoidal commutation provides smoother torque output but suffers from efficiency loss at higher speeds. Vectorial control offers the best performance by maintaining constant torque but is complex and expensive to implement due to the need for real-time rotor position detection and mathematical transformations like Clarke and Park. Simulations conducted in MATLAB/Simulink demonstrated the performance of open and closed-loop control for BLDC motors, using PI control to regulate speed. From this paper, we learned how different commutation techniques impact torque quality, speed control, and overall motor performance, helping inform the selection of appropriate control methods in BLDC motor applications.

Aspalli *et al.* [12] provided an in-depth analysis of the design and implementation of a cost-effective speed control system for a BLDC motor using a Four-Switch Three-Phase Inverter (FSTPI) controlled by a dsPIC30F4011 digital signal controller. The study addresses the reduction of switching losses and

electromagnetic interference (EMI) while maintaining effective speed control. Unlike the traditional six-switch inverter, the FSTPI configuration reduces circuit complexity by using only four switches, lowering hardware cost and power loss. Rotor position is detected using three Hall-effect sensors, enabling proper commutation. The system is simulated in MATLAB/Simulink and verified through hardware implementation. Both open-loop and closed-loop control strategies are tested, showing close agreement between simulation and experimental results. From this paper, we learned how the combination of a simplified inverter topology and digital control can achieve reliable and efficient BLDC motor operation, particularly in low-cost embedded applications like EVs and industrial drives.

Kumar *et al.* [13] analyzed the design and simulation of a solar-powered water pumping system using a BLDC motor drive, modeled and analyzed in MATLAB/Simulink. The system integrates a solar PV array, DC-DC boost converter, and a voltage source inverter (VSI) to run a centrifugal water pump via a BLDC motor. A major contribution of the paper is the elimination of current sensing components in the motor control loop by using a DC link voltage regulator and PWM control, which reduces system cost and complexity. The use of the Incremental Conductance (IN-C) MPPT algorithm ensures maximum power extraction from the PV array under varying atmospheric conditions. From this study, we learned how effective integration of MPPT, efficient converter design, and sensorless speed control enables a reliable and low-cost solution for standalone solar-powered BLDC irrigation systems, especially in remote and agricultural areas.

Mohanraj *et al.* [14] presents a comprehensive review of the current state-of-the-art in BLDC motor technology. The paper addresses critical challenges in BLDC motor applications, such as fault tolerance, electromagnetic interference, torque ripple, and acoustic noise. It emphasizes the importance of advanced control techniques like Field-Oriented Control (FOC), Direct Torque Control (DTC), and Model Predictive Control (MPC), while also discussing the impact of structural design on performance. This work helped us understand the range of control methods available and their importance in achieving high-performance, noise-reduced, and reliable motor operation across diverse applications like electric vehicles and pumping systems.

Kumar *et al.* [15] investigates closed-loop speed control of a BLDC motor using both conventional and modified PID controllers. The novelty of their work lies in designing a modified PID based on dominant pole placement to reduce overshoot and improve tracking performance under load disturbances. MATLAB/Simulink simulations are used to evaluate torque, speed, and back-EMF behavior. This paper provided key insights into controller selection and highlighted the performance limitations of traditional PID, motivating the use of enhanced techniques for better transient and steady-state performance.

Suganthi *et al.* [16] explores the modeling and simulation of BLDC motor speed control using both PID and fuzzy logic controllers. The authors emphasize the superior dynamic response of fuzzy-based control, particularly under varying load conditions. They implemented a hybrid control strategy using MATLAB/Simulink, showing improved speed regulation, reduced overshoot, and better robustness compared to conventional methods. This study informed us on the advantages of intelligent control techniques and provided a benchmark for evaluating classical vs. soft-computing approaches in real-time BLDC applications.

Chapter-III

System Components

3 System components

3.1 Inverter

A three-phase voltage-source inverter (VSI) operating in 120° conduction mode energizes each phase for 120 electrical degrees while leaving it open-circuited for the remaining 60°. This method is particularly advantageous in BLDC motor drives, as it simplifies the commutation process and minimizes the overlapping of conduction states. Each switching action produces a line-to-line voltage pulse that aligns with the rotor's trapezoidal back-EMF, enhancing torque production. The switching logic is governed by Hall sensor signals or estimated rotor positions in sensorless drives. Accurate modeling of the inverter includes both the conduction and commutation intervals, often handled using Average-Value Models (AVMs), which can predict system behavior in both the time and frequency domains [17]. The mathematical representation of the output line-to-line voltage V_{ab} for 120° conduction mode can be expressed as:

$$V_{ab} = V_{DC} \times \text{Switching Function},$$

where the switching function is determined by the Hall sensor logic.
Additionally, the phase voltage equations can be described as:

$$V_A = R_s I_A + L_s \frac{dI_A}{dt} + E_A$$

$$V_B = R_s B_B + L_s \frac{dI_B}{dt} + E_B$$

$$V_C = R_s I_C + L_s \frac{dI_C}{dt} + E_C$$

And the line-to-line voltages as:

$$V_{AB} = V_A - V_B$$

$$V_{BC} = V_B - V_C$$

$$V_{CA} = V_C - V_A$$

In a star connection, line-to-neutral voltages relate to line voltages as:

$$V_{AN} = \frac{2V_{AB} + V_{BC}}{3}$$

$$V_{BN} = \frac{-V_{AB} + V_{BC}}{3}$$

$$V_{CN} = \frac{-V_{AB} - 2V_{BC}}{3}$$

Gate driver:
The gate driver acts as an interface between the microcontroller or digital signal processor (DSP) and the high-power switching devices (MOSFETs or IGBTs) in the inverter. It amplifies the logic-level PWM signals and provides necessary isolation through opto-isolators or magnetic isolators. The driver prevents shoot-through conditions by incorporating dead-time control and also influences the rise and fall times of gate signals, which in turn affects switching losses and electromagnetic interference (EMI). Advanced gate drivers support fault detection and desaturation protection [18].

3.2 Hall position sensor

Three Hall-effect sensors are strategically placed 120 electrical degrees apart around the stator to detect rotor magnetic field transitions. Each sensor outputs a digital signal that transitions based on the rotor pole passing by. These signals are critical for identifying the correct commutation sector. The resulting 3-bit Hall code generates six distinct states, enabling unambiguous determination of the rotor's position every 60 electrical degrees [19].

Hall decoder:
The Hall decoder interprets the three-bit Hall signal (Ha, Hb, Hc) and maps it to six unique gate control signals (g1–g6). These signals determine the switching states of the inverter legs. A truth table defines this mapping, ensuring only two switches are ON at a time, avoiding short-circuit paths. Misalignment or improper mounting of Hall sensors causes positional error, leading to distorted torque waveforms. Calibration techniques or mathematical compensation methods such as lookup tables are used to mitigate these effects [19][20].

3.3 Back EMF

Back electromotive force (EMF) is generated as the rotor magnets sweep past the stator windings. For BLDC motors, this waveform is ideally trapezoidal and given by:

$$E_{ph}(t) = k_e \cdot \omega(t),$$

where k_e is the back EMF constant and $\omega(t)$ is the rotor speed. The undriven phase is monitored during its 60° off interval to detect the zero-crossing point of the back EMF, which is used in sensorless control strategies [19][21]. This method allows the controller to infer rotor position without physical sensors.

The voltage equation considering back EMF for any phase can be rewritten as:

$$V_Y = E_A + R_s i_A$$

3.4 Line currents

The phase currents in 120° conduction mode are non-sinusoidal and discontinuous. Each phase conducts for only 120°, resulting in flat-topped or quasi-trapezoidal current profiles. The line current i_a for one phase during its conduction period can be approximately described by:

$$i_a(t) = \frac{V_{dc} - E_A(t)}{R + L\frac{d}{dt}},$$

where R and L are the stator resistance and inductance, and $E_a(t)$ is the corresponding back EMF. These waveforms induce torque ripple, which can be mitigated by smoothing filters or current averaging control [22].

3.5 Electromagnetic torque

The electromagnetic torque T_e in a BLDC motor is the result of the interaction between the phase current and back EMF and is given by:

$$T_e = \frac{1}{\omega} \sum_{i=A}^{C} E_i(t) \cdot i_i(t),$$

where $E_i(t)$ and $i_i(t)$ are the back EMF and current for each phase. While the ideal torque should remain constant, practical systems experience ripple due to delays in switching and finite current slopes during commutation [18][23]. This ripple can be minimized using advanced commutation strategies or torque compensation algorithms.

3.6 Mechanical system

The mechanical dynamics of the rotor are governed by Newton's second law:

$$J\frac{d\omega}{dt} = T_e - T_L$$

$$J\frac{d\omega}{dt} + B\omega = T_e - T_L$$

where J is the moment of inertia, B is the damping coefficient, ω is angular velocity, T_e is electromagnetic torque, and T_L is the load torque. Solving this differential equation provides insight into system stability, acceleration profiles, and transient responses [24]. Integration of this equation in MATLAB/Simulink allows performance evaluation under variable load conditions.

3.7 Angle converter

In low-cost BLDC motor drives, the 6-step hall sensor output is insufficient for high-resolution speed control or vector control methods. The angle converter transforms this into a quasi-continuous angle using interpolation techniques or sensorless observers. For instance, a linear interpolator or a PLL (phase-locked loop) can estimate intermediate positions between transitions. This angle can then feed into advanced controllers like FOC, which require precise rotor position [21][25].

3.8 PI controller

In the initial stage of BLDC motor control, a classical Proportional-Integral (PI) controller is implemented to regulate the motor speed in a closed-loop configuration. This method continuously adjusts the torque applied to the motor by calculating the error between the reference speed and the actual rotor speed and minimizing it over time. The PI controller generates a control signal based on the proportional and integral components of this error, which then modulates the inverter's output to maintain desired performance. This ensures smooth acceleration, stable operation, and reduced steady-state speed error. The controller operates by fine-tuning the stator current to indirectly influence torque, thereby correcting any speed deviations. This approach is widely used due to its simplicity, ease of implementation, and effectiveness under linear operating conditions [14]. While it may not account for non-linearities or external disturbances inherently, the PI controller provides a reliable and responsive method for speed control in most standard BLDC motor applications [15][16].

3.9 Hardware System Components

The hardware implementation of the BLDC motor control system involves the following key components:

- **BLDC hub motor:** An IS48 1200W BLDC hub motor equipped with three Hall sensors (H1, H2, H3) and three phase wires (Yellow, Green, Blue) is used. The commutation sequence is determined based on digital Hall signals—an established method for precise phase switching in BLDC drives [26]
- **Hall sensors:** Digital Hall-effect sensors mounted at 120° intervals within the motor provide rotor position signals. These are powered via a 12V DC supply (Red = +12V, Black = GND). Fault-detection algorithms are often integrated to ensure reliable commutation in industrial implementations [27]
- **dSPACE 1104 controller:** The dSPACE DS1104 real-time controller reads Hall sensor inputs via digital I/O, and executes Simulink-based control logic. It also generates PWM gate signals for inverter switching—a validated rapid prototyping approach in many published setups [28]
- **Gate driver circuit:** A dedicated amplifier circuit, powered from an 18V transformer, boosts the DS1104's digital outputs to drive IGBTs or MOSFETs in the inverter reliably and safely.
- **Inverter:** A three-phase Voltage Source Inverter (VSI) receives gate pulses and converts a 48V DC input (via an auto-transformer) into three-phase AC for stator excitation. This architecture closely follows typical BLDC drive design [29]

- **Power supply:** The BLDC motor is powered from a regulated 48V DC supply, while the inverter gate driver uses an 18V transformer. The auto transformer provides auxiliary power as needed.
- **Measurement tools:** An oscilloscope monitors motor voltage and current waveforms. Measured motor RMS voltage is approximately 32V and current is around 3.5A under test conditions, consistent with published experimental values [30]

Chapter-IV

Methodology and system architecture

4 Methodology

4.1 Open-loop 120° conduction control

Open-loop control of a BLDC motor in six-step (120°) conduction mode uses predefined inverter switching without real-time rotor feedback. At any instant, two phases conduct current while the third is floating. Accurate modeling of the motor behavior in this mode requires consideration of electrical, magnetic, and mechanical dynamics.

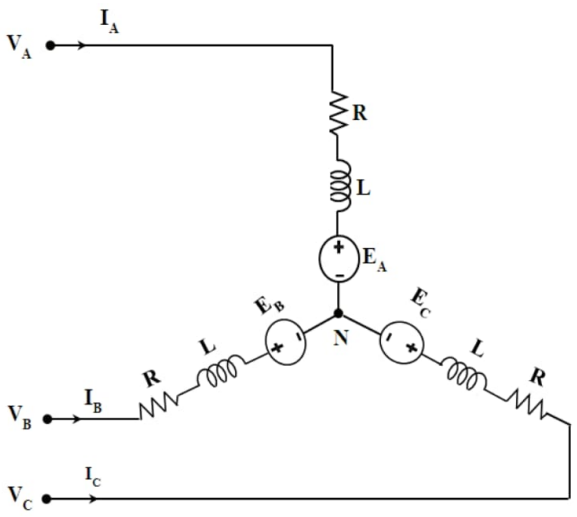

Fig. 2: Equivalent circuit of BLDC motor

Equivalent phase model: Each motor phase can be modeled using:

$$V_x = R_x I_x + E_{\psi.x}$$

Where:

- V_x = Phase voltage
- I_x = Phase current
- R_x = Phase resistance
- $E_{\psi.x}$ = Induced back-EMF in phase $x = A, B, C$

Phase voltage equations: The individual phase equations accounting for mutual inductance M and self-inductance L are:

$$V_A = R_s I_A + L \cdot \frac{dI_A}{dt} + E_A - M \cdot \frac{dI_A}{dt} \Rightarrow V_A = R_s I_A + (L - M)\frac{dI_A}{dt} + E_A$$

$$E_A = \frac{d\Psi}{dt}$$

Define effective inductance as $L_s = L - M$:

$$V_A = R_s I_A + L_s \frac{dI_A}{dt} + E_A \tag{1}$$

Similarly:

$$V_B = R_s I_B + L_s \frac{dI_B}{dt} + E_B \tag{2}$$

$$V_C = R_s I_C + L_s \frac{dI_C}{dt} + E_C \tag{3}$$

Line-to-line voltage relations:

$$V_{AB} = V_A - V_B \tag{4}$$

$$V_{BC} = V_B - V_C \tag{5}$$

$$V_{CA} = V_C - V_A \tag{6}$$

From these, phase voltages can be rewritten:

$$V_A = \frac{2V_{AB} + V_{BC}}{3} \tag{7}$$

$$V_B = \frac{-V_{AB} + V_{BC}}{3} \tag{8}$$

$$V_C = \frac{-V_{AB} - 2V_{BC}}{3} \tag{9}$$

Line currents: From equation (1):

$$\frac{dI_A}{dt} = \frac{1}{L_s}(V_A - E_A - R_s I_A)$$

From equation (7):

$$\frac{dI_A}{dt} = \frac{1}{3L_s}[2V_{AB} + V_{BC} - 3R_s I_A - 3E_A] \Rightarrow I_A = \int \frac{1}{3L_s}[2V_{AB} + V_{BC} - 3R_s I_A - 3E_A]dt$$

Similarly:

$$I_B = \int \frac{1}{3L_s}[-V_{AB} + V_{BC} - 3R_s I_B - 3E_B]dt$$

Star connection constraint:

$$I_C = -I_A - I_B$$

Trapezoidal back-EMF:

$$E_A = K_e \cdot \omega_e \cdot f(\theta) \tag{10}$$

$$E_B = K_e \cdot \omega_e \cdot f(\theta - \frac{2\pi}{3}) \tag{11}$$

$$E_C = K_e \cdot \omega_e \cdot f(\theta - \frac{4\pi}{3}) \tag{12}$$

Electromagnetic torque:

$$T_e = \frac{T_A + T_B + T_C}{\omega_m}$$

$$= \frac{1}{\omega_m}(E_A I_A + E_B I_B + E_C I_C)$$

$$T_e = P \cdot \Phi_m(\Psi_A I_A + \Psi_B I_B + \Psi_C I_C)$$

Mechanical dynamics:

$$T_e = J\frac{d\omega_m}{dt} + B\omega_m + T_L \tag{13}$$

$$\frac{d\omega_m}{dt} = \frac{1}{J}(T_e - T_L - B\omega_m) \tag{14}$$

$$\omega_m = \int \frac{1}{J}(T_e - T_L - B\omega_m)dt \tag{15}$$

Rotor electrical angle:

$$\theta_e = \int \frac{P}{2}\omega_m dt$$

Theta (°)	H1	H2	H3	A	B	C
-180 to -120	0	0	1	-1	0	1
-120 to -60	1	0	1	0	-1	1
-60 to 0	1	0	0	1	-1	0
0 to 60	1	1	0	1	0	-1
60 to 120	0	1	0	0	1	-1
120 to 180	0	1	1	-1	1	0

Table 2: BLDC commutation table (theta: -180° to 180°)

Commutation table (six-step 120°):

Table explanation: Each row represents a 60° sector of rotor electrical angle and maps the Hall sensor values (H1, H2, H3) to the active phase switching states:

- **+1** → High-side switch ON (positive bus)
- **-1** → Low-side switch ON (ground)
- **0** → Floating (both switches OFF)

In this six-step logic:

- Two phases conduct, and one floats.
- The pattern rotates every 60° electrical, ensuring proper alignment of stator field with rotor magnets.
- Each conducting phase remains ON for 120° and OFF for 60°, creating a $+ + 0 - - 0$ pattern.
- Floating phase's back-EMF zero-crossing can be used for sensorless control.

Additional technical notes:

- The generated torque is proportional to the overlap of current and back-EMF in the conducting phases.
- The shape of the back-EMF (trapezoidal) and current pulse leads to torque ripple at the commutation edges.
- Despite ripple, this method offers simplicity and reliability in many applications such as fans, e-bikes, and small robots.

This section presents a complete dynamic model of BLDC motor operation under 120° open-loop conduction, integrating voltage, current, torque, and rotor motion equations with switching logic for practical implementation.

4.2 Flowchart

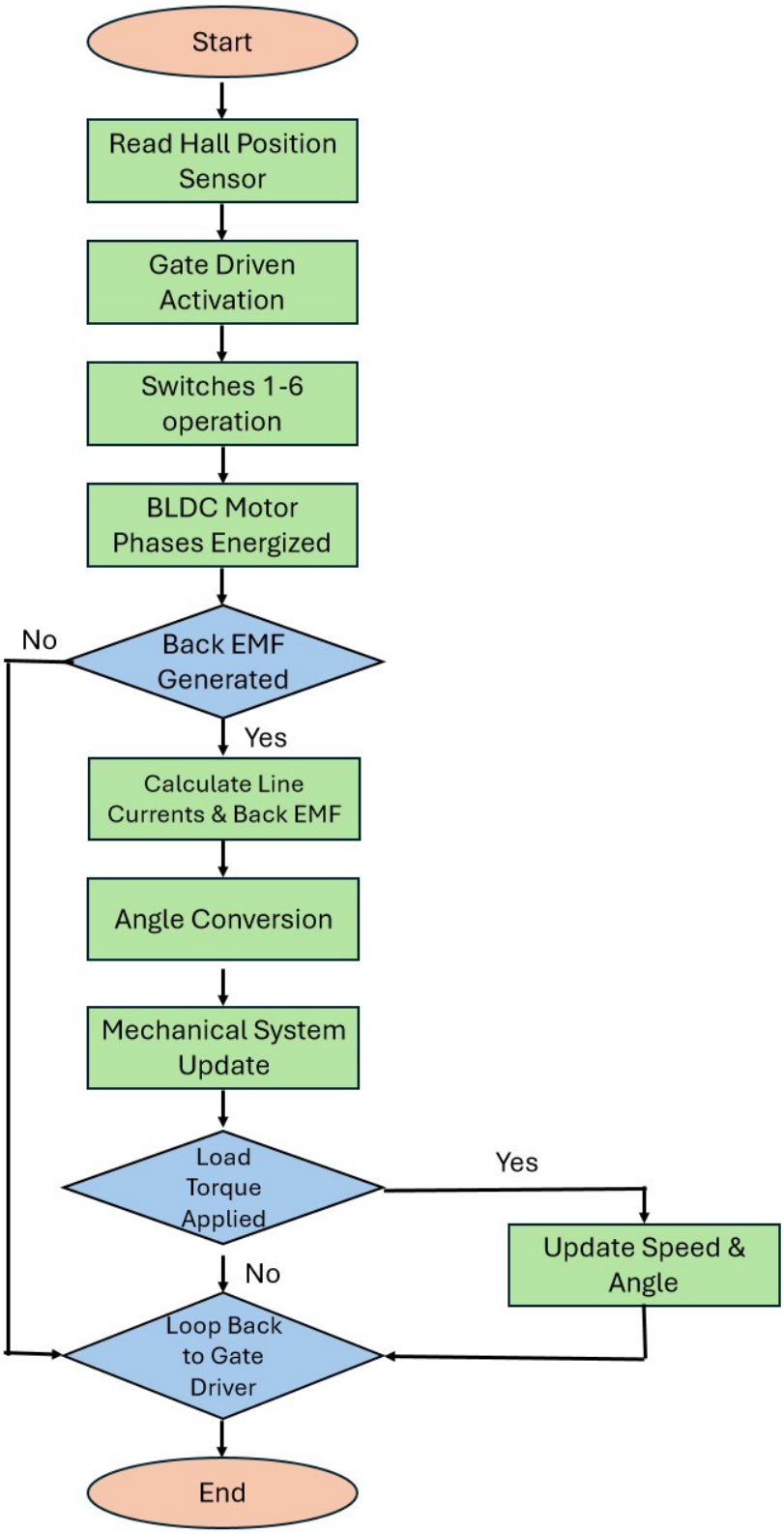

Fig. 3: Flow chart for open loop BLDC motor

4.3 System architecture

The system architecture describes the modular design of the BLDC motor simulation model, implemented in MATLAB/Simulink. It represents the sequence of computational blocks used to simulate the motor's electrical and mechanical behavior under an open-loop six-step (120°) commutation scheme.

Although the control logic is open-loop—meaning there is no real-time feedback from output variables to the inverter— the overall simulation still forms a natural physical loop. This is because the motor's internal dynamics are interdependent: the rotor speed determines the electrical angle, which affects the back-EMF, influencing current and torque, which again changes the speed.

The main blocks of the architecture include:

- **Back-EMF block:** Computes the trapezoidal back-EMFs E_A, E_B, and E_C based on rotor electrical angle θ_e and speed ω_m.
- **Complete mathematical modeling block:** Solves the phase voltage equations to obtain instantaneous currents based on applied voltages, resistance, inductance, and back-EMFs.
- **Line current block:** Integrates the current differential equations to compute I_A, I_B, and I_C while enforcing the star-connection constraint ($I_A + I_B + I_C = 0$).
- **Electromagnetic torque block:** Calculates torque T_e as a function of back-EMFs and line currents.
- **Mechanical system block:** Computes rotor acceleration and speed using Newton's second law, considering torque, damping, and load.
- **Angle converter block:** Integrates rotor speed ω_m to determine electrical angle θ_e, which is fed back to the back-EMF block.

The interconnection of these blocks is shown in the system block diagram (see Fig. 4). This architecture provides a complete and modular representation of the BLDC motor's internal dynamics under open-loop simulation.

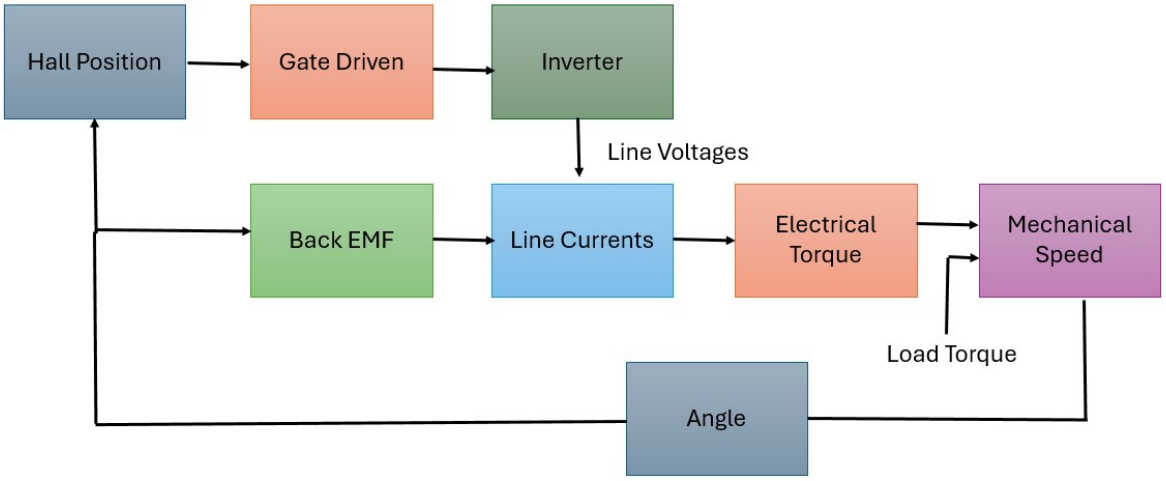

Fig. 4: System architecture of open-loop BLDC motor simulation

4.4 Closed-Loop Speed Control using PI Controller

Speed Error Calculation The instantaneous speed error $e(t)$ is computed as:

$$e(t) = \omega_{\text{ref}}(t) - \omega_{\text{actual}}(t)$$

where:

- ω_{ref}: Reference speed (rad/s or RPM)
- ω_{actual}: Measured rotor speed from the motor

PI Controller Equation The PI controller uses the error signal to compute the electromagnetic torque T_e as:

$$T_e(t) = K_p \cdot e(t) + K_i \int_0^t e(\tau)\, d\tau$$

where:

- K_p: Proportional gain
- K_i: Integral gain
- $T_e(t)$: Torque command used as input to the motor

Working Principle The torque generated by the PI controller is directly applied to the motor via the inverter. This simple yet effective control scheme ensures that the motor accelerates or decelerates to match the reference speed. The feedback loop continuously corrects any deviation by adjusting the torque.

4.5 Hardware methodology

The motor control methodology implemented is based on sensor-based commutation using hall signals. The overall control strategy is outlined as follows:

- **Hall signal acquisition:** The BLDC motor's hall sensors generate a 3-bit binary signal corresponding to rotor position, which is read through the digital inputs of dSPACE 1104.
- **Commutation logic:** A lookup table-based hall decoder in simulink determines the appropriate gate signals for the inverter switches according to the rotor position.
- **Gate signal generation:** Based on the hall decoder output, gate signals are generated using logic blocks and routed to the digital outputs of dSPACE 1104.
- **Amplification:** These signals are amplified using an external circuit to ensure sufficient gate voltage and current to drive the inverter's IGBT or MOSFET switches.
- **Power flow:** A 3-phase supply from an auto-transformer powers the inverter, while the inverter's output drives the three-phase input of the motor.

Chapter-V

Implementation

5 Implementation

5.1 Overview

The mathematical model of the BLDC motor, as derived in earlier sections, is implemented in MATLAB/Simulink. This simulation replicates the dynamic behavior of the motor system by incorporating electrical, electromagnetic, and mechanical subsystems. The modeling approach is based on literature and verified equations drawn from prior work [31, 32].

5.2 Electrical subsystem

Each stator phase is modeled as a series R–L circuit with a back-EMF component, represented by the following differential equations:

$$V_A = R_s I_A + L_s \frac{dI_A}{dt} + E_A$$
$$V_B = R_s I_B + L_s \frac{dI_B}{dt} + E_B$$
$$V_C = R_s I_C + L_s \frac{dI_C}{dt} + E_C$$

These are implemented in Simulink using integrators and sum blocks. Each back-EMF E_x is calculated as a function of rotor angle.

5.3 Back-EMF block

Back-EMF waveforms are modeled as trapezoidal signals synchronized with rotor electrical position:

$$E_A = K_e \omega_e f(\theta)$$
$$E_B = K_e \omega_e f\left(\theta - \frac{2\pi}{3}\right)$$
$$E_C = K_e \omega_e f\left(\theta - \frac{4\pi}{3}\right)$$

where K_e is the back-EMF constant, and $f(\theta)$ is the waveform shape.

5.4 Inverter and commutation logic

A six-switch VSI inverter is implemented with gate signals generated from decoded Hall effect sensor logic. The switching sequence corresponds to 120° conduction logic. The Hall decoder converts signals (H1, H2, H3) into six gate pulses used to drive the inverter switches. This system simulates a real-time BLDC inverter circuit.

5.5 Electromagnetic torque

The instantaneous electromagnetic torque is calculated by:

$$T_e = \frac{1}{\omega_m}(E_A I_A + E_B I_B + E_C I_C)$$

This equation is simulated by multiplying phase currents and back-EMF, followed by summation and division.

5.6 Mechanical system

The mechanical motion is governed by:

$$J\frac{d\omega_m}{dt} + B\omega_m = T_e - T_L$$

Where:

- J: moment of inertia,
- B: damping coefficient,
- T_e: electromagnetic torque,
- T_L: load torque.

This system is modeled using a transfer function block or integrator to get speed and position.

5.7 Angle converter

To generate rotor electrical position θ, the mechanical speed is integrated and scaled:

$$\theta_e = \int \omega_m dt \cdot \frac{P}{2}$$

Where P is the number of poles. This output is used in the back-EMF generator and Hall sensor emulator.

5.8 Simulink architecture

The complete model includes:

- Trapezoidal back-EMF generator
- Hall sensor decoder
- Six-switch inverter
- Electrical phase circuit (R–L + EMF)
- Mechanical dynamics calculator

Oscilloscope blocks display outputs such as torque, current, rotor speed, and back-EMF.

5.9 Simulation parameters

The values used in simulation are adapted from motor datasheets and IEEE literature

- $R_s = 3.2\,\Omega$
- $L_s = 8\,\text{mH}$
- $K_e = 1.5 \times P \times \Phi\, V \cdot s/\text{rad}$
- $J = 0.6 \times 10^{-6}\,\text{kg} \cdot \text{m}^2$
- $B = 1.0 \times 10^{-6}\, N \cdot m \cdot s$
- $V_{DC} = 110\, V$
- $T_L = 5\, Nm$
- $P = 6$
- $\Phi = 0.11\, Wb$

This implementation forms a verified simulation model that allows detailed dynamic analysis of BLDC motors. The results from this simulation are validated in the next chapter.

5.10 Outer Loop Controller

The outer loop controller in the BLDC motor simulation serves as the speed regulation layer. It compares the actual motor speed with the reference speed and generates the torque demand required to drive the motor accordingly. This controller is essential in ensuring that the motor achieves and maintains the desired speed under different operating conditions.

The outer loop controller consists of the following functional blocks:

- **Reference Speed Input:** A predefined signal (step or ramp) indicating the desired speed of the motor. It acts as the setpoint for the system.
- **Speed Feedback:** The actual rotor speed is obtained from the motor's mechanical model or a speed estimation algorithm and fed back into the controller.
- **Error Calculation:** The difference between the reference speed and the actual speed is calculated to determine the deviation.

$$e(t) = \omega_{\text{ref}}(t) - \omega_{\text{actual}}(t)$$

- **PI Controller:** A proportional-integral (PI) controller processes the error signal to generate the required electromagnetic torque T_e.

$$T_e(t) = K_p \cdot e(t) + K_i \int e(t)\, dt$$

  This torque command is passed to the inner loop or mathematical motor model, where it governs the motor's acceleration.

- **Torque Limiter (Optional):** A saturation block may be used after the PI controller to limit the maximum torque, protecting the motor from overcurrent during large speed errors.

5.11 Hardware implementation

The experimental hardware setup was implemented as follows:

- The IS48 BLDC hub motor was powered by a 48 V DC regulated power supply. The hall sensors were powered separately using a 12 V DC source.
- Hall sensor outputs (H1, H2, H3) were connected to digital input pins of the dSPACE 1104 controller board. The simulink model reads these signals in real-time.
- Inside simulink, a logic builder (hall decoder) translates the Hall codes into gate drive logic.
- The decoded gate pulses are routed to digital outputs of dSPACE 1104. These outputs are connected to a gate driver amplifier circuit, powered by an 18 V transformer.
- The amplified signals drive the gates of a three-phase inverter circuit. The inverter is powered by a 3-phase auto-transformer to produce AC signals suitable for BLDC excitation.
- The three-phase output of the inverter is then connected directly to the motor windings (Yellow, Green, Blue wires).
- Speed, voltage, and current readings were observed using an oscilloscope. RMS output voltage was 32 V and load current reached approximately 3.5 A.

Chapter-VI

Results and Analysis

6 Simulation and results

6.1 Simulation

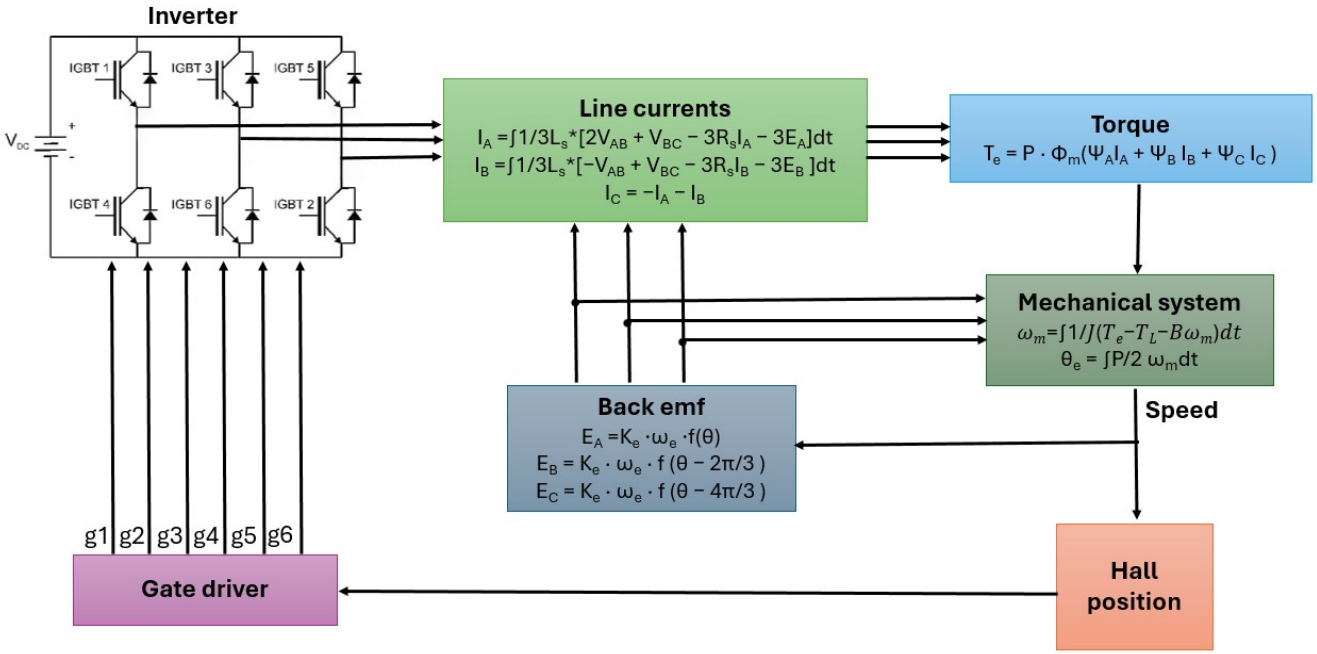

Fig. 5: Simulation block diagram

The block diagram illustrates the complete outer-loop simulation architecture for a Brushless DC (BLDC) motor drive system. The inverter consists of six IGBT switches controlled by gate pulses (g_1–g_6) from the gate driver, which receives commutation signals based on Hall sensor inputs. These Hall sensors provide rotor position information but are not used in a feedback control loop — instead, they enable appropriate switching sequences in a predefined manner.

The inverter generates line-to-line voltages (V_{AB}, V_{BC}), which are used to compute line currents (I_A, I_B, I_C) through differential equations involving stator resistance, inductance, and back-EMF. The back-EMF for each phase is a function of rotor electrical angle and speed, and is generated by trapezoidal functions. The resulting phase currents and EMFs contribute to the electromagnetic torque T_e, which drives the mechanical subsystem.

The mechanical system calculates rotor speed (ω_m) and electrical angle (θ_e) using the dynamic torque equation. These values are then used to update the back-EMF and simulate the Hall position signals. Since this is an open-loop system, there is no feedback loop to automatically correct speed or torque. Instead, motor performance relies solely on the predefined switching logic and Hall-based commutation, making it simpler but more susceptible to load variations and disturbances.

Complete mathematical modeling: The mathematical modelling block is the core computational block of the system that implements the voltage equations using the inputs: rotor electrical angle θ_e,

back-EMFs E_A, E_B, E_C, and voltage supply. It solves:

$$V_k = R_s I_k + L_s \frac{dI_k}{dt} + E_k, \quad k \in \{A, B, C\}$$

It outputs the phase currents I_A, I_B, I_C required for torque and mechanical computation.

Back EMF block: The back EMF block generates the trapezoidal back-EMF signals for all three phases:

$$E_k = K_e \cdot \omega_e \cdot f(\theta_k)$$

where each E_k is a function of the rotor electrical position and contributes to torque calculation and phase voltage equations.

Electromagnetic torque block: Torque is derived using the given below equation:

$$T_e = P \cdot \Phi_m(\Psi_A I_A + \Psi_B I_B + \Psi_C I_C)$$

The given expression relates the electromagnetic work done per second based on instantaneous currents and back-EMF.

Mechanical system block: The mechanical system block integrates the net torque to obtain motor speed:

$$J\frac{d\omega_m}{dt} + B\omega_m = T_e - T_L$$

The given equation simulates the rotor's acceleration and frictional losses.

Angle converter block: The angle converter block calculates the electrical angle of the rotor from the mechanical speed using the given equation:

$$\theta_e = \int \frac{P}{2}\omega_m \, dt$$

The given electrical angle is used by the Back-EMF generator to maintain a proper commutation sequence.

System loop summary: The output of the angle converter drives the back-EMF generator, which feeds into the mathematical model to compute voltages and currents. These currents determine torque, which updates the rotor speed and position forming a self-sustained simulation loop.

Closed loop PI controller: The outer loop PI controller maintains the speed of the motor by dynamically adjusting the torque input based on system feedback. It is especially important during changes in reference speed or when the motor experiences sudden load variations.

6.2 Hardware simulation

The implemented Simulink model was designed to perform real-time commutation based on Hall signal input using the dSPACE 1104 board. The simulation was tested on hardware under a constant 48 V DC supply.

- **Commutation Logic Validation:** The 3-bit Hall signal input successfully selected the appropriate switching pattern to generate six-step commutation.
- **Gate Signal Observation:** The dSPACE-generated signals were clearly observed at the inverter gates and exhibited expected switching intervals.

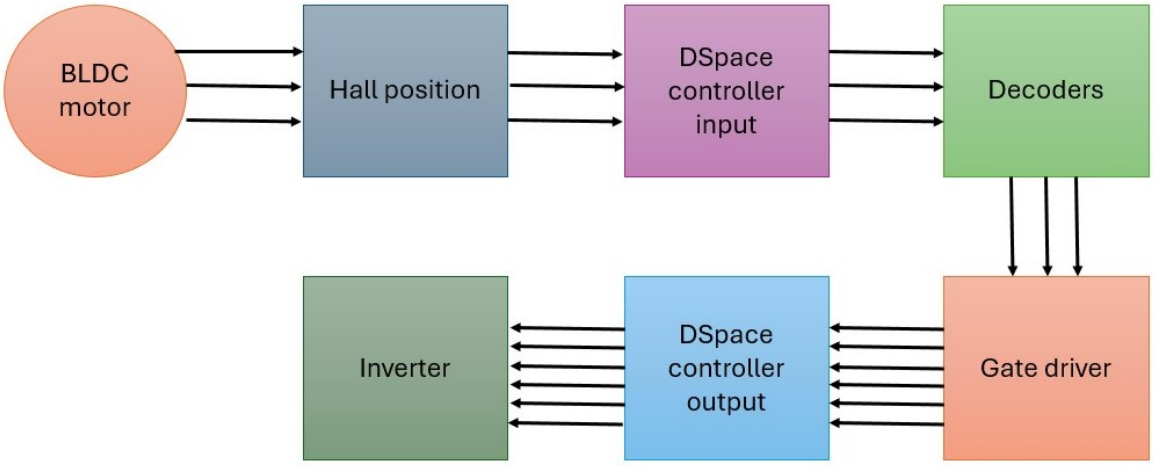

Fig. 6: Logic for hardware setup

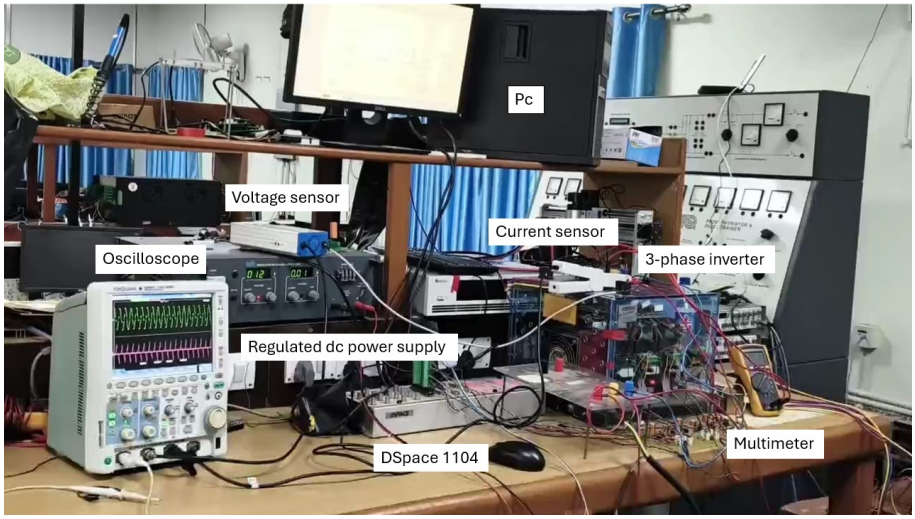

Fig. 7: Experimental bench

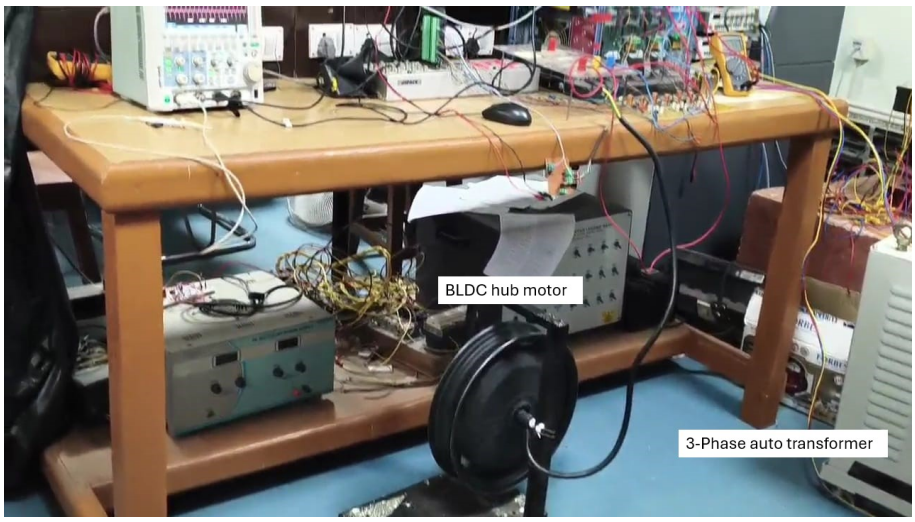

Fig. 8: Experimental bench

6.3 Result

The following plots illustrate the simulation output of the open-loop and closed-loop BLDC motor model. Each figure corresponds to a key dynamic or electrical parameter derived from the mathematical modeling and simulation blocks.

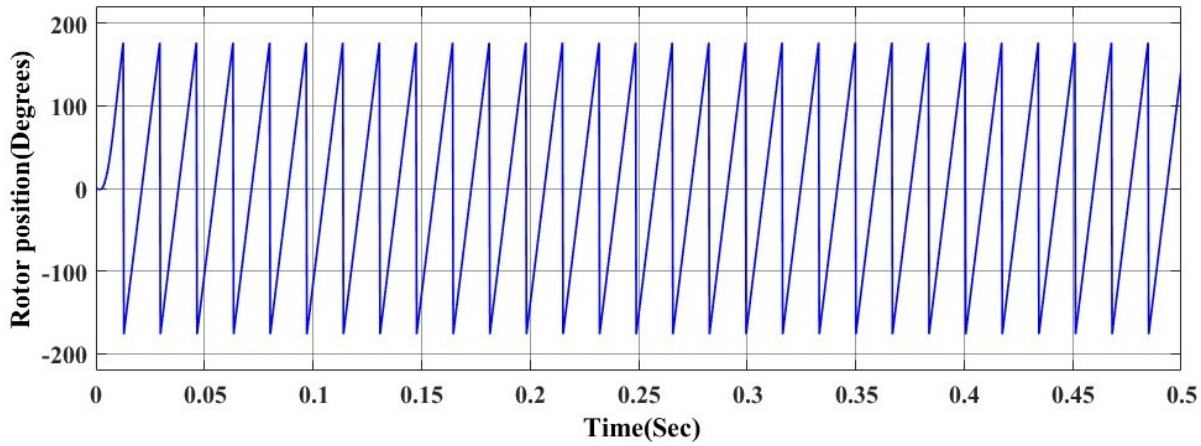

Fig. 9: Rotor electrical angle vs time

Angle Response: The rotor electrical angle vs time plot shows the evolution of the rotor's electrical angle θ_e over time, which is computed by integrating the mechanical angular velocity. A smooth ramp indicates correct feedback and commutation logic. The linear growth of θ_e confirms uniform acceleration under applied torque and stable electrical synchronization. This angle is crucial for aligning inverter switching states with rotor position in both open-loop and closed-loop control. Any distortion or nonlinearity in this plot could indicate issues with speed estimation, integration error, or improper sampling of Hall signals.

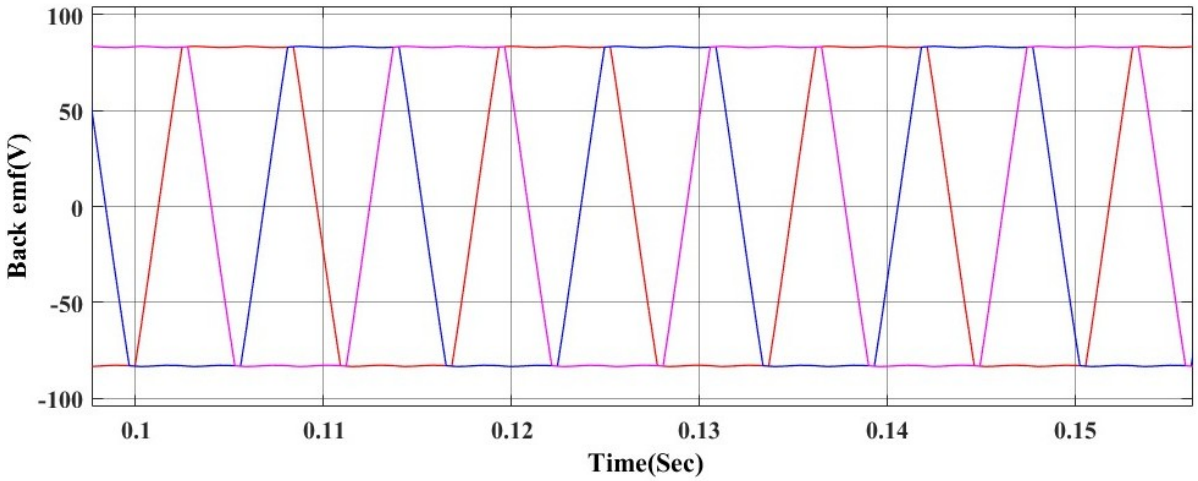

Fig. 10: Back EMF (trapezoidal)

Back EMF: The complete back EMF for all phases shows back-EMFs E_A, E_B, and E_C over one full electrical cycle. The 120° phase displacement and consistent trapezoidal shape validate correct alignment with rotor angle and electrical frequency. The waveforms confirm the ideal back-EMF profile expected from a BLDC motor with surface-mounted permanent magnets. These EMFs are crucial for generating electromagnetic torque and are directly proportional to rotor speed. Accurate back-EMF modeling is essential for both torque prediction and sensorless control techniques such as back-EMF zero-crossing detection. All three waveforms start and end at the same voltage levels, preserving phase symmetry and ensuring consistent integration across one electrical cycle.

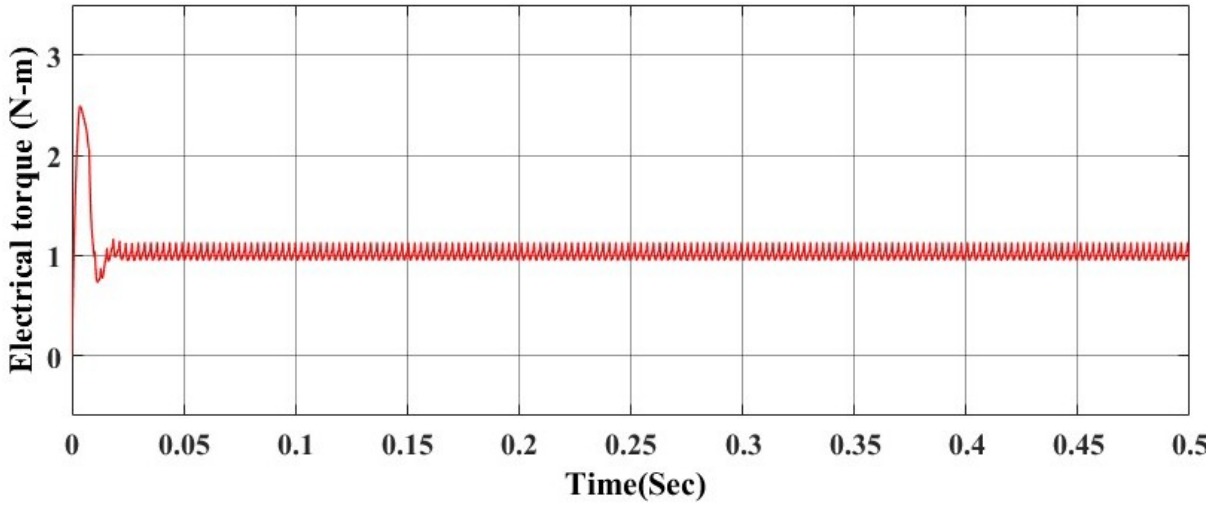

Fig. 11: Electromagnetic torque

Torque Output: Torque is calculated from the cross product of current and back-EMF. The waveform shows ripple inherent in 120° conduction mode, but average torque remains stable. This ripple occurs due to the discontinuous conduction of one phase during each 60° interval. Despite the ripple, the motor maintains sufficient average torque to drive the load effectively. The torque profile closely aligns with the timing of the switching sequence, confirming correct commutation and current alignment with back-EMF. Improved torque smoothness could be achieved with advanced techniques like Field-Oriented Control (FOC) or DTC. However, for many applications, the performance of six-step commutation is adequate and offers a simpler hardware implementation.

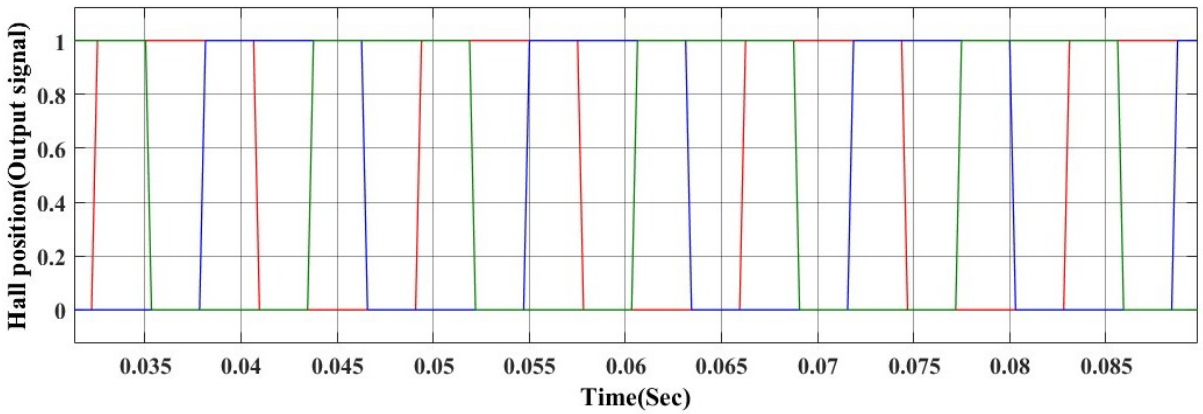

Fig. 12: Hall sensor position signals

Hall Position Logic: The digital output of the three Hall sensors (H1, H2, H3) is shown. Each transitions every 60°, forming the basis for commutation logic in open-loop control. These signals represent discrete rotor positions and are decoded into sector numbers to drive the inverter switches. The sequence follows a 6-step pattern, ensuring that the correct phases are energized at the right time. Accurate decoding of Hall signals is crucial for maintaining synchronism between the stator field and the rotor movement, ensuring continuous torque production. The use of digital Hall sensors simplifies the control strategy and eliminates the need for rotor position estimation. Any misalignment or delay in Hall transitions can directly affect torque smoothness and introduce commutation errors.

These signals also serve as key inputs for generating PWM signals in real-time hardware systems. In practical implementations, signal filtering and debounce logic are sometimes employed to mitigate electrical noise. Proper placement of the sensors on the stator is critical to minimize phase lag and maximize dynamic performance.

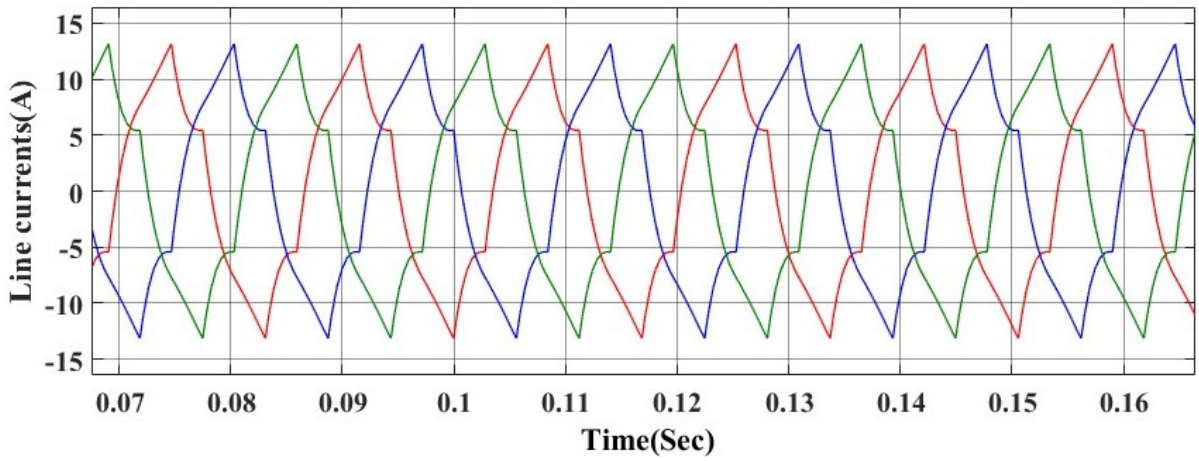

Fig. 13: Line currents

Line Currents: Current flows in two phases at any time, with the third floating, creating characteristic trapezoidal waveforms. This validates the conduction pattern from the commutation table. The active phases conduct for 120° electrical degrees, ensuring that the torque-producing components of the current align with the back-EMF. The floating phase shows the back-EMF waveform undistorted, which is often used in sensorless control for zero-cross detection. The transitions between conduction intervals result in sharp edges in the current waveform, contributing to torque ripple. Despite these discontinuities, the overall current pattern confirms proper sector-wise switching. Such waveform analysis is crucial for validating inverter logic and detecting any phase misalignment or hardware faults. The periodicity and symmetry of the waveforms also help confirm the correct decoding of Hall signals. Additionally, consistent current amplitude across sectors reflects proper DC link voltage and healthy phase impedance balance.

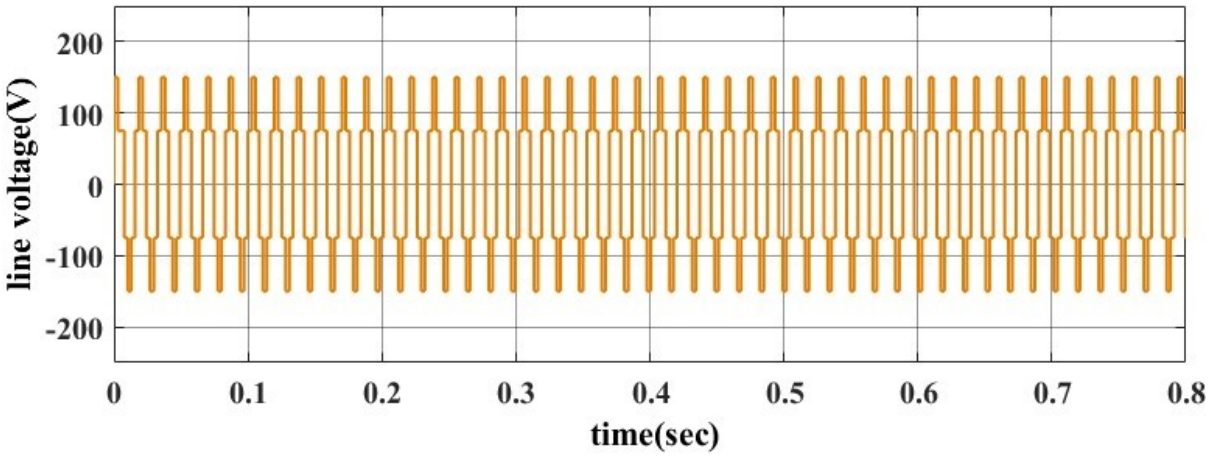

Fig. 14: Line voltages

Line Voltages: Line-to-line voltages V_{AB}, V_{BC}, V_{CA} show square-wave patterns consistent with six-step inverter operation. These align with rotor positions and switching intervals. Each voltage waveform remains constant over a 60° electrical interval before switching to the next level, indicating proper commutation timing. The voltage transitions are synchronized with Hall sensor changes, ensuring continuous rotation. The amplitude of the line voltages reflects the applied DC bus voltage and the inverter's switching logic. These waveforms confirm that the inverter is correctly generating the expected excitation for trapezoidal back-EMF BLDC motors. The symmetry of the voltage levels across each pair of phases validates the balanced nature of the motor drive. Deviations or distortion in these waveforms can signal inverter faults or incorrect timing. Monitoring line voltages is therefore essential for both debugging and performance optimization in real-time motor control.

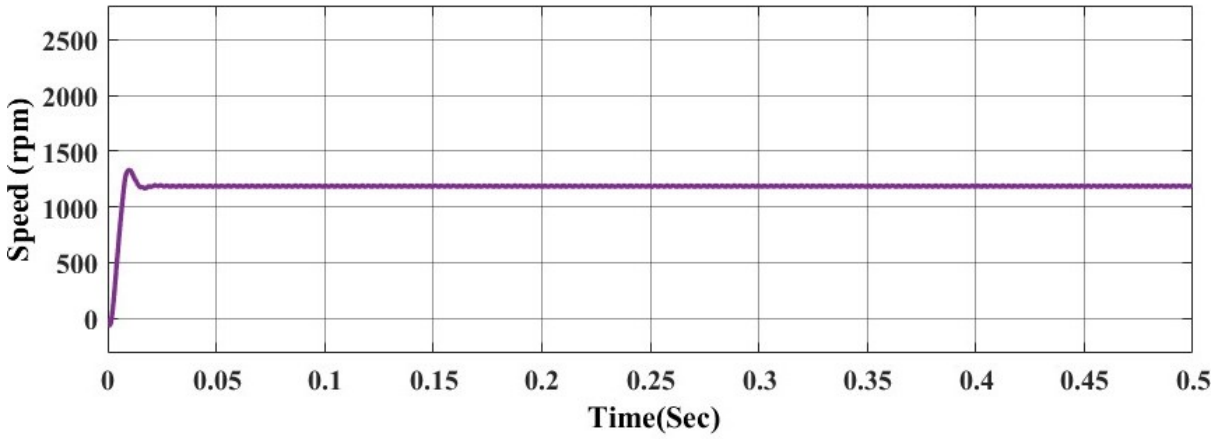

Fig. 15: Mechanical speed

Rotor mechanical speed: This plot shows the gradual acceleration of the rotor until steady-state is reached. It reflects system inertia, friction, and net torque dynamics. The motor begins from standstill and ramps up as torque builds, governed by the differential equation $J\frac{d\omega_e}{dt} + B\omega_e = T_e - T_L$. The smooth rise indicates that the applied torque overcomes the combined effects of load and damping. Under PI control, the motor tracks the reference speed with minimal overshoot and fast settling time. Any deviation from the setpoint is corrected as the controller adjusts the voltage accordingly. Once the net torque equals the opposing load torque, speed stabilizes at the commanded value. This dynamic profile validates both the mechanical model and control loop accuracy.

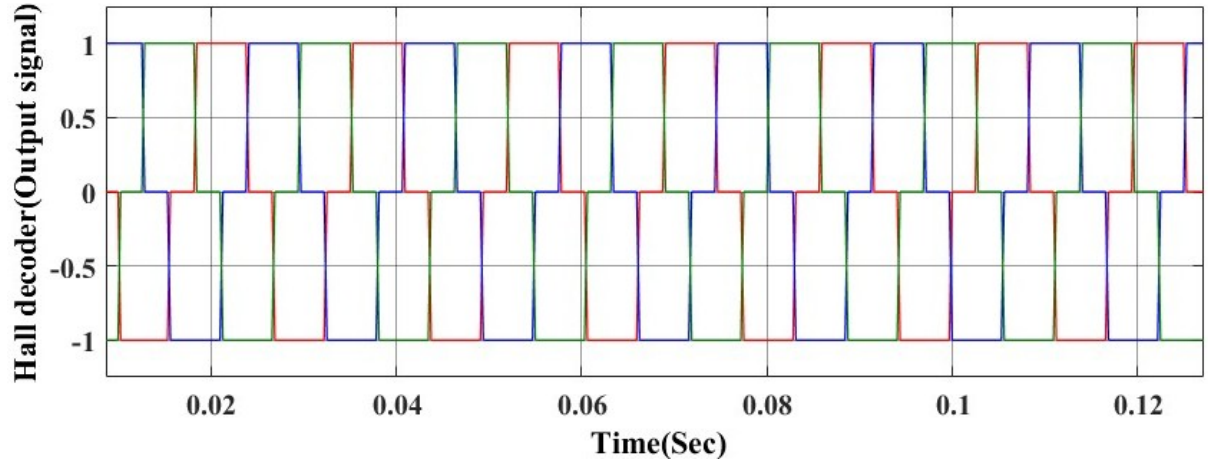

Fig. 16: Phase voltages

Phase voltages: The phase voltages (A, B, C) show typical inverter output with transitions occurring at 60° intervals. The waveform indicates correct PWM-based switching logic and timing. Each phase is energized for 120° with a flat-topped voltage pulse, while the remaining 60° corresponds to a floating or inactive state. The voltages are phase-shifted by 120° to produce a rotating magnetic field in the stator. These patterns confirm accurate implementation of six-step commutation based on Hall signal decoding. Voltage symmetry across all three phases reflects balanced inverter operation and proper pulse-width modulation. Any distortion or asymmetry could indicate switching faults or incorrect commutation sequencing.

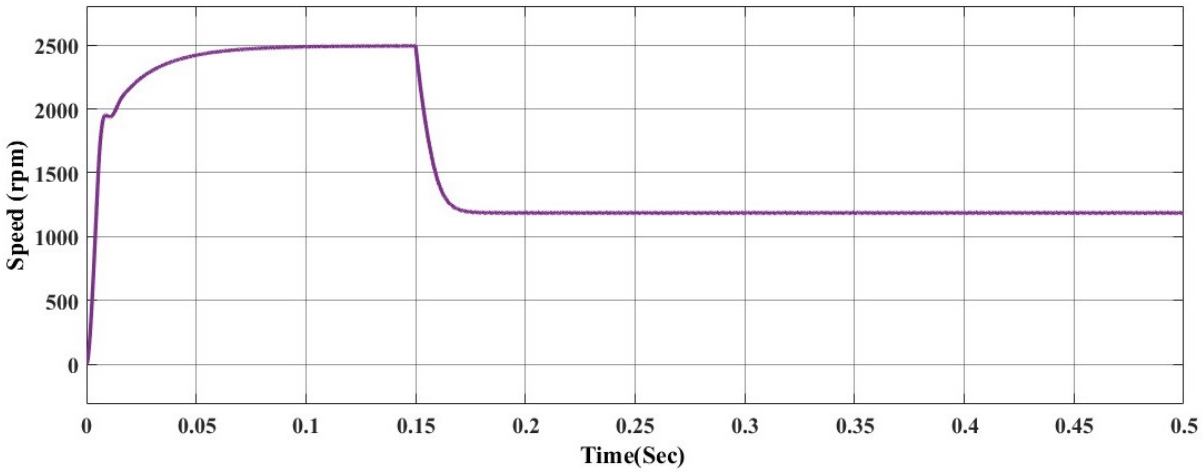

Fig. 17: Rotor speed response (load applied at $t \approx 0.15$ sec)

Rotor speed – load disturbance analysis: The above figure presents the dynamic rotor speed response of the BLDC motor under open-loop control. Initially, the motor operates under *no-load condition*, resulting in a smooth acceleration and stabilization around a peak speed close to 500 rad/s. This matches the expected behavior for an open-loop system where torque directly controls acceleration until countered by frictional and back-EMF forces. At approximately $t \approx 0.18$ seconds, a *load torque is suddenly applied* to the motor shaft. The effect of this external disturbance is clearly observed as a *sharp drop in rotor speed*, reflecting the sudden increase in opposing torque.

Following this drop, the motor stabilizes to a *new steady-state speed* of approximately 300 rad/s. The mild oscillations observed during the transition indicate that the system absorbs the load effect with minor transient ripples, after which the damping and friction balance the electromagnetic torque.
This validates the motor response to external load without any feedback regulation, showing the importance of torque reserve in open-loop applications.

Key Observations:

- The initial rise represents free acceleration in no-load.
- The load causes a transient dip but the system stabilizes.
- No oscillatory instability is observed, indicating good torque–inertia balance.

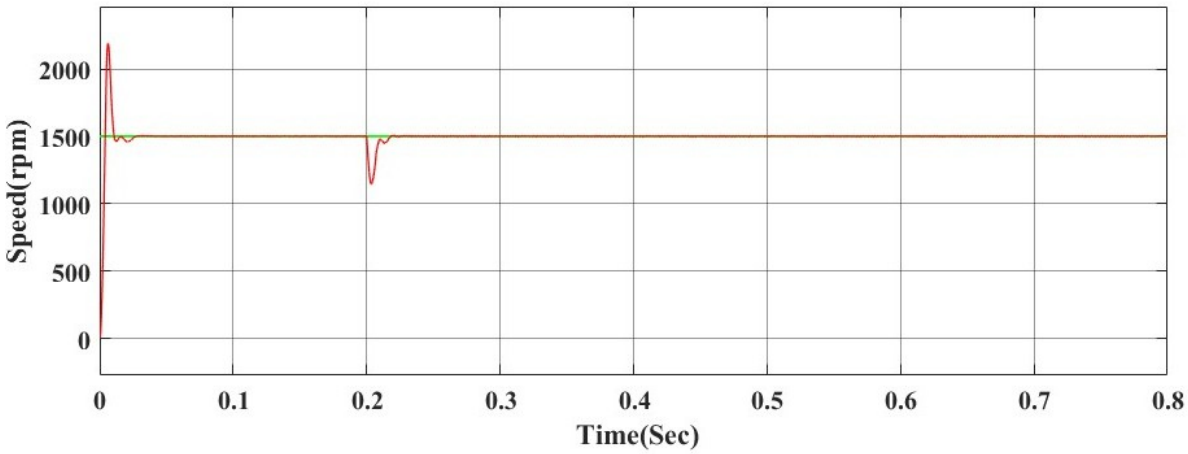

Fig. 18: Actual speed

PI-based closed-loop speed control: The simulation was performed for two speed steps: an initial reference of 750 RPM and a step increase to 1500 RPM at 0.3 seconds. At $t = 0.2$ seconds, a mechanical load is applied to the motor, causing a temporary drop in speed. However, the PI controller responds effectively by increasing the torque, and the motor speed returns to the reference value of 750 RPM after a brief transient. This demonstrates the controller's ability to restore steady-state operation even under load disturbances. The full response is shown in Fig. 18

6.4 Hardware results

Motor Performance: Upon connection, the motor ran smoothly with measured RMS voltage of 32 V and an RMS current of 3.5 A. Commutation transitions were clearly reflected in the phase voltage and current waveforms.

Oscilloscope Readings: Waveforms captured using the oscilloscope showed consistent trapezoidal phase voltages and pulsed phase currents consistent with 120° conduction mode.

Noise and Ripple: The current waveform exhibited minor ripple due to switching transients but remained within safe operating range.

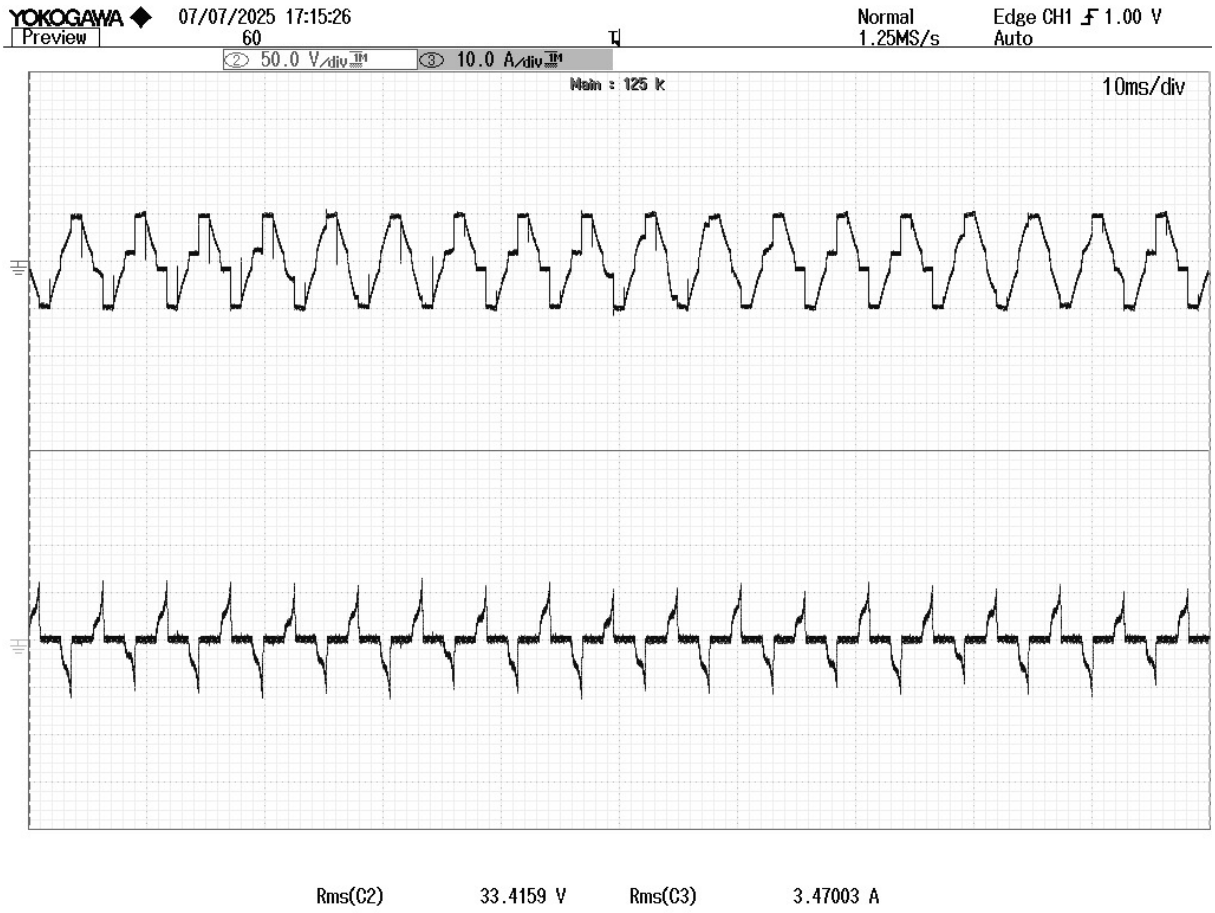

Fig. 19: Oscilloscope readings

6.5 Real-time simulation and hardware verification using OPAL-RT

To validate the open-loop control model of the BLDC motor under practical operating conditions, a real-time simulation was performed using the OPAL-RT system. The model, initially developed in MATLAB/Simulink, was configured for deployment using RT-LAB's real-time execution framework, enabling hardware-in-the-loop (HIL) interaction and real-time observation of system dynamics.

The real-time simulation was conducted under two distinct load scenarios:

1. **No-Load Condition:** In this case, the motor operated without any mechanical load. The speed response was smooth and reached steady-state as expected. The line current waveforms showed minimal load-induced ripple, and torque generation corresponded primarily to frictional and inertial resistance. This served as a baseline for verifying correct commutation logic and electrical dynamics.

2. **Loaded Condition (50% Load):** A mechanical load equivalent to 50% of the motor's rated torque was applied. Given the rated torque of 5 N-m for the BLDC motor, a load torque of 2.5 N-m was introduced in the simulation. Under this load, the motor exhibited a slight dip in speed during transient response, but due to the applied voltage and switching pattern, it recovered and stabilized close to the expected operating point. The electromagnetic torque increased proportionally to counteract the load, validating the torque generation model under dynamic conditions.

Both test scenarios were monitored using scopes integrated in the RT-LAB interface, capturing real-time speed, torque, current, and voltage signals. The system confirmed stable operation in both cases, and the open-loop model demonstrated robustness under the applied conditions.

These results confirm that the simulated open-loop controller functions correctly in real-time environments. Moreover, this real-time verification lays the groundwork for transitioning to closed-loop strategies such as PI control or advanced Direct Torque Control (DTC) for performance enhancement in future implementations.

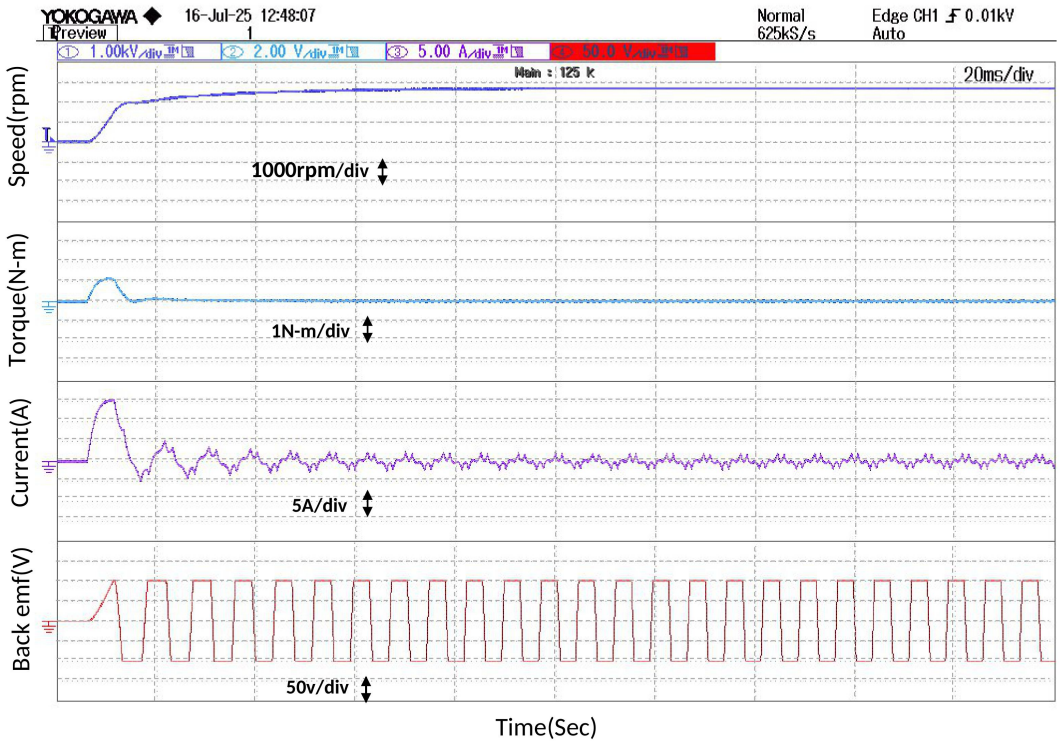

Fig. 20: No load measurements of open loop BLDC motor

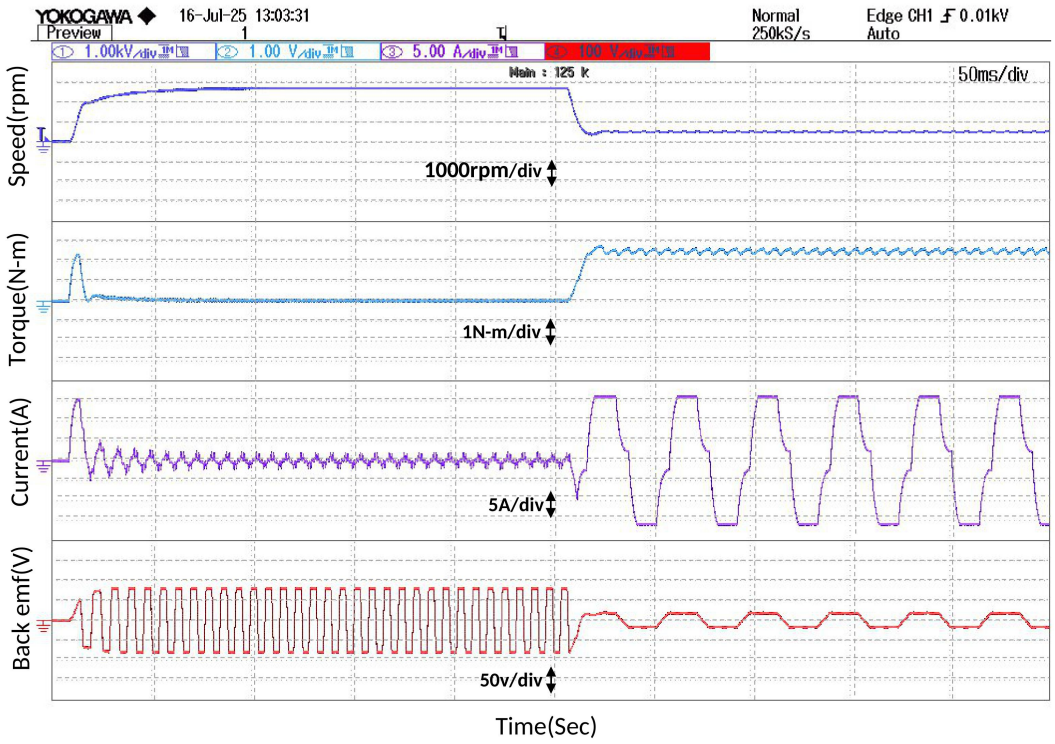

Fig. 21: 50% loaded measurements of open loop BLDC motor

6.6 Observations

The complete modeling, simulation, and hardware validation of the BLDC motor under both open-loop and PI-based closed-loop control provided several critical insights into motor dynamics, inverter performance, and control strategy robustness.

Open-Loop Behavior: In the open-loop configuration, inverter switching relied solely on Hall sensor feedback without any dynamic error correction. The six-step 120° commutation successfully energized two phases at any given time while the third floated. The resulting phase voltages and line currents showed expected trapezoidal and quasi-square patterns, confirming correct inverter logic. However, electromagnetic torque exhibited noticeable ripple, and speed regulation was not possible under load. The motor failed to maintain desired speed when subjected to disturbances, revealing the limitation of open-loop operation in dynamic environments.

Closed-Loop PI Control: The addition of a PI controller in the outer loop brought significant performance improvements. The motor was subjected to two-speed steps (750 RPM and 1500 RPM) and a step load of 2.5 Nm (50% of rated torque) was applied at 0.2 s. The motor initially tracked 750 RPM with minimal overshoot. After load application, the speed dropped briefly, but the PI controller compensated and restored the setpoint. The dynamic response was stable with a fast settling time and negligible steady-state error. The ability to maintain speed under load validated the effectiveness of closed-loop control and proper tuning of K_p and K_i.

Hall Sensor Decoding and Commutation Logic: The three Hall sensors (H1, H2, H3) produced digital signals spaced at 120°, enabling precise sector identification every 60°. These signals were fed into a decoding logic built in Simulink, which converted them into sector numbers. The sector outputs were then used to generate gate signals using lookup tables. The gate sequence maintained proper switching alignment with rotor position, ensuring correct commutation and continuous torque production. There were no signal glitches, and the simulation logic matched hardware behavior.

Back-EMF Alignment and Switching: Simulated back-EMF profiles followed an ideal trapezoidal waveform, with each phase leading or lagging by 120°. These EMFs were in-phase with their correspond-

ing phase currents during conduction intervals. The floating phase provided a clear back-EMF waveform, useful for sensorless control and zero-cross detection in future work. Back-EMF amplitudes scaled with rotor speed, and transitions matched inverter switching events, confirming the accuracy of the model.

Line Currents and Torque Behavior: Line currents in simulation and experiment showed the typical six-step pattern with conduction over 120° intervals and rest over the remaining 240°. The third phase floated and tracked the EMF waveform. Current polarity reversed every 180° electrical, producing unidirectional torque. The torque waveform exhibited periodic ripple due to phase switching, but average torque was sufficient to overcome load. No irregularities were observed in current rise time, peak levels, or symmetry, validating both inverter logic and phase balancing.

Rotor Speed Tracking: Speed response closely matched the reference profile during both no-load and load conditions. The PI-controlled system successfully transitioned from 750 RPM to 1500 RPM and maintained performance despite torque disturbances. Under open-loop control, however, the system was sensitive to load and failed to self-correct. The real-time response in dSPACE matched the simulation plots, indicating proper tuning of PI gains and fidelity of the simulation model.

Hardware Implementation using dSPACE 1104: The dSPACE DS1104 controller served as the core platform for signal interfacing and real-time execution. Hall sensor signals (Yellow, Green, Blue) were fed into digital inputs, and decoded signals drove gate control logic in Simulink. The output pulses were amplified using an 18 V gate driver and connected to the inverter. A 3-phase auto-transformer supplied the inverter. Final motor outputs were observed on an oscilloscope. The motor achieved 32 V RMS output and drew an average of 3.5 A under 48 V DC supply, consistent with simulated performance. The response under real-time constraints showed no instability or delay, validating model reliability and control robustness.

Overall Insights and Future Scope: The experimental outcomes confirm that the open-loop system is functional but limited in regulation capability. The closed-loop PI controller significantly enhanced stability, precision, and load-handling. The Hall-based commutation logic worked reliably in both simulation and hardware. The project successfully bridges the gap between mathematical modeling, simulation, and hardware realization. With the base framework in place, the system is now ready to incorporate more advanced control algorithms such as Direct Torque Control (DTC) or sensorless estimation techniques for improved torque ripple suppression and dynamic performance.

6.7 Conclusion

This report presents a comprehensive modeling, simulation, and real-time implementation framework for a three-phase Brushless DC (BLDC) motor, encompassing both open-loop and closed-loop PI control strategies. Initially, an analytical model was derived using the fundamental voltage, current, and torque equations. The mathematical framework integrated subsystems such as trapezoidal back-EMF generation, line current derivation, electromagnetic torque estimation, and rotor mechanical dynamics. A six-step commutation method based on 120° conduction was implemented using sector decoding from Hall sensor signals.

The open-loop Simulink model verified correct sector switching and current conduction patterns through simulation of line voltages, line currents, and back-EMF. Rotor angle and torque profiles showed alignment with commutation timing, and electromagnetic torque exhibited the expected ripple due to discontinuous conduction. While the motor accelerated correctly and tracked rotor dynamics under no-load conditions, it lacked adaptability to load variations, highlighting the limitations of open-loop systems.

To overcome this, a Proportional-Integral (PI) controller was designed and introduced in the outer speed loop. The controller dynamically modulated the torque-producing current in response to speed error. Simulation results under varying reference speeds and applied loads confirmed closed-loop stability and effective speed regulation. Specifically, a step reference from 750 RPM to 1500 RPM and load introduction at 0.2 s demonstrated that the motor could maintain desired speed with minimal overshoot and rapid recovery, showcasing the controller's robustness.

In the hardware phase, real-time implementation was performed using a 1200 W IS48 BLDC hub motor and dSPACE 1104 controller. The Hall signals were acquired through dSPACE digital I/O pins and decoded in Simulink to identify the current electrical sector. Gate pulses were generated accordingly and passed through an amplifier circuit before driving a 3-phase inverter. The inverter was powered by a 3-phase auto-transformer, and oscilloscope monitoring confirmed RMS output of 32 V and a current draw of approximately 3.5 A under 48 V DC supply.

The success of Hall decoding, gate signal generation, and sector-wise commutation was validated in both simulation and experimental domains. The decoder accurately tracked rotor position transitions every 60°, enabling precise control of the inverter phases. Amplifier and gate driver circuits proved effective in maintaining signal integrity between low-voltage logic outputs and high-voltage switching hardware.

Closed-loop speed control using the PI controller was experimentally tested under both no-load and 50% load conditions. When the 2.5 Nm load (out of a 5 Nm rated torque) was applied at 0.2 s, the motor experienced a temporary speed dip, which was quickly corrected by the controller, restoring equilibrium at 750 RPM. This response demonstrated real-world effectiveness of the controller in handling dynamic disturbances and verified simulation accuracy.

At the simulation level, all modeling blocks—including back-EMF generation, current integration, torque computation, mechanical speed estimation, and angle conversion—were independently validated and integrated. Simulation outputs such as angle ramp, line currents, torque ripple, and Hall sensor signals matched real-time behavior, building strong confidence in model fidelity and controller implementation.

In conclusion, this project successfully bridges theoretical motor modeling, simulation-based validation, and hardware-in-the-loop implementation using dSPACE 1104. The developed control architecture is modular, scalable, and hardware-ready, serving as a valuable platform for future work. Upcoming improvements will include advanced strategies such as Direct Torque Control (DTC), Field-Oriented Control (FOC), and sensorless control using back-EMF zero-crossing or observers. These enhancements will further improve torque smoothness, efficiency, and responsiveness—making the system suitable for high-performance industrial drives and electric mobility applications.

References

[1] S. Sakunthala, R. Kiranmayi, P. N. Mandadi, A study on industrial motor drives: Comparison and applications of pmsm and bldc motor drives, in: 2017 International Conference on Energy, Communication, Data Analytics and Soft Computing (ICECDS), IEEE, 2017, pp. 537–540.

[2] S. Lakshmikanth, R. Devarajaiah, A. Chowdhury, S. Krishna, Analytical design of 3kw bldc motor for electric vehicle applications, in: 2023 3rd International Conference on Intelligent Technologies (CONIT), IEEE, 2023, pp. 1–7.

[3] P. Yedamale, Brushless dc (bldc) motor fundamentals, Microchip Technology Inc 20 (1) (2003) 3–15.

[4] Y. Zheng, Z. Cao, S. Wang, Comparative study of bldc motor modeling, in: 2018 Australian New Zealand Control Conference (ANZCC), 2018, pp. 62–64. doi:10.1109/ANZCC.2018.8606596.

[5] M. Poovizhi, M. S. Kumaran, P. Ragul, L. I. Priyadarshini, R. Logambal, Investigation of mathematical modelling of brushless dc motor(bldc) drives by using matlab-simulink, in: 2017 International Conference on Power and Embedded Drive Control (ICPEDC), 2017, pp. 178–183. doi:10.1109/ICPEDC.2017.8081083.

[6] T. Sithananthan, A. Bakar, H. Poad, S. Salimin, Design and simulation of dc-dc buck-boost converter with voltage source inverter using matlab/simulink for bldc motor drives, in: 2024 IEEE 4th International Conference in Power Engineering Applications (ICPEA), 2024, pp. 107–111. doi:10.1109/ICPEA60617.2024.10498714.

[7] S. N. L, A. S, T. S. Babu, R. R. S, V. S. S, Closed-loop speed control of bldc motor using flyback converter for electric vehicle applications, in: 2024 International Conference on E-mobility, Power Control and Smart Systems (ICEMPS), 2024, pp. 1–6. doi:10.1109/ICEMPS60684.2024.10559343.

[8] Yadunandan, B. Naik, R. Konduru, A. Karni, S. Kalligudd, Modelling of bldc motor foc and hardware implementation using f28069m launchpad, in: 2023 International Conference on Next Generation Electronics (NEleX), 2023, pp. 1–5. doi:10.1109/NEleX59773.2023.10420991.

[9] V. S. Bondre, A. G. Thosar, Mathematical modeling of direct torque control of bldc motor, in: 2017 International Conference on Innovative Research In Electrical Sciences (IICIRES), 2017, pp. 1–8. doi:10.1109/IICIRES.2017.8078304.

[10] S. Burman, M. Dubey, Design an efficient cuk converter for a bldc motor drive, in: 2022 International Conference on Intelligent Controller and Computing for Smart Power (ICICCSP), 2022, pp. 1–7. doi:10.1109/ICICCSP53532.2022.9862508.

[11] S. A. R. Sierra, J. F. M. Carballido, J. L. V. González, Switching techniques for brushless dc motors, in: CONIELECOMP 2013, 23rd International Conference on Electronics, Communications and Computing, 2013, pp. 162–166. doi:10.1109/CONIELECOMP.2013.6525779.

[12] M. S. Aspalli, F. M. Munshi, S. L. Medegar, Speed control of bldc motor with four switch three phase inverter using digital signal controller, in: 2015 International Conference on Power and Advanced Control Engineering (ICPACE), 2015, pp. 371–376. doi:10.1109/ICPACE.2015.7274975.

[13] M. Kumar, P. Deosarkar, R. Mahanty, Design and development of bldc motor drive for solar-pv irrigation system using matlab, in: 2023 IEEE International Students' Conference on Electrical, Electronics and Computer Science (SCEECS), 2023, pp. 1–4. doi:10.1109/SCEECS57921.2023.10063109.

[14] D. Mohanraj, R. Aruldavid, R. Verma, K. Sathiyasekar, A. B. Barnawi, B. Chokkalingam, L. Mihet-Popa, A review of bldc motor: state of art, advanced control techniques, and applications, Ieee Access 10 (2022) 54833–54869.

[15] B. Kumar, S. K. Swain, N. Neogi, Controller design for closed loop speed control of bldc motor, International Journal on Electrical Engineering and Informatics 9 (1) (2017) 146.

[16] P. Suganthi, S. Nagapavithra, S. Umamaheswari, Modeling and simulation of closed loop speed control for bldc motor, in: 2017 Conference on Emerging Devices and Smart Systems (ICEDSS), IEEE, 2017, pp. 229–233.

[17] Q. Han, N. Samoylenko, J. Jatskevich, Average-value modeling of brushless dc motors with 120° voltage source inverter, IEEE Transactions on Energy Conversion 23 (2) (2008) 423–432. doi:10.1109/TEC.2008.918628.

[18] T. Instruments, Sensorless trapezoidal control of bldc motors using back emf detection, https://www.ti.com/lit/an/slyt501/slyt501.pdf (2015).

[19] T. E. E. GmbH, Bldc motor drive fundamentals, https://toshiba.semicon-storage.com/ (2018).

[20] A. Zaher, K. Atallah, D. Howe, Influence of hall sensor misalignment on the performance of brushless dc motors, IEEE Transactions on Magnetics 42 (10) (2006) 3504–3506. doi:10.1109/TMAG.2006.879650.

[21] U. H. Lee, T. Youn, J. Lee, How to model brushless electric motors for lightweight robotic systems, IEEE Access 11 (2023) 24709–24720. doi:10.1109/ACCESS.2023.3254091.

[22] MathWorks, Bldc motor control with hall sensors - simulink example, https://www.mathworks.com/help/sps/ug/bldc-motor-control-with-hall-sensors.html (2022).

[23] H. Atighechi, View of average-value modeling of 120° vsi commutated brushless dc motors, ResearchGatehttps://www.researchgate.net/publication/224425163 (2009).

[24] T. Murali, R. Arulmozhiyal, Investigation of a sensorless bldc drive using matlab simulink and fpga, International Journal of Power Electronics and Drive Systems 12 (3) (2021) 1889–1896. doi:10.11591/ijpeds.v12.i3.pp1889-1896.

[25] R. E. Corporation, Bldc motor control using 120° commutation mode, https://www.renesas.com/us/en/document/apn/120-degree-commutation-bldc (2021).

[26] T. H. Kim, M. Ehsani, Sensorless control of bldc motors from near-zero to high speeds, IEEE Transactions on Power Electronics 19 (6) (2004) 1635–1645. doi:10.1109/TPEL.2004.836625.

[27] J. Cervantes, E. Cordova, A. I. S. Marrufo, I. U. P. Monarrez, M. Nandayapa, Bldc motor commutation based on dsp builder for fpga, in: 2016 International Power Electronics Congress (CIEP), 2016, pp. 166–171. doi:10.1109/CIEP.2016.7530750.

[28] A. F. A. Zaidi, S. A. Azmi, L. J. Hwai, K. Kamarudin, et al., dspace implementation of motor drives using asymmetric converter, Journal of Advanced Research in Applied Sciences and Engineering Technology 33 (3) (2024) 51–61. doi:10.37934/araset.33.3.5161.

[29] G. Mihalache, A. D. Ioan, Fpga implementation of bldc motor driver with hall sensor feedback, 2018 European Conference on Power Electronics and Applications (2018) 624–629doi:10.1109/EPE.2018.8559886.

[30] S. Maheshwari, V. Jain, R. Saini, Experimental performance analysis of bldc motor using real-time oscilloscope monitoring, IEEE Transactions on Instrumentation and Measurement 68 (5) (2019) 1525–1533. doi:10.1109/TIM.2018.2869385.

[31] A. Tatar, E. Ayaz, H. Ayaz, A dynamic analysis of bldc motor by using matlab/simulink and mathematica, in: 2017 International Conference on Engineering and Technology (ICET), 2017, pp. 1–6. doi:10.1109/ICEngTechnol.2017.8308190.

[32] Anonymous, Mechanical system modeling of bldc motors, accessed from internship archive (Mechanical system.pdf) (2022).